Investigation on Accuracy of Numerical Simulation of Aerodynamic Noise of Single-stage Axial Fan

Huabing Lu [a,b], Youhong Xiao [a,*], Zhigang Liu [a], Ye Yuan [a], Peilin Zhou [b,*], Guanghui Yang [a]

[a] College of Power and Energy Engineering, Harbin Engineering University, Harbin, China.

[b] Department of Naval Architecture, Ocean & Marine Engineering, University of Strathclyde, Glasgow, United Kingdom.

*Corresponding author:
Youhong Xiao, Institution: Harbin Engineering University. Address: NO.145-1 Nantong Street, Nangang District, Harbin City, Heilongjiang Province, China. Email: xiaoyouhong@hrbeu.edu.cn.

Peilin Zhou, Institution: University of Strathclyde. Address: 16 Richmond Street, Glasgow G1 1XQ, United Kingdom. Email: Peilin.zhou@Strath.ac.uk.

Abstract

The prediction accuracy of turbomachinery aerodynamic noise, particularly in relation to broadband noise with uncertain factors, has long been a challenging issue. Previous studies have not fully comprehended the factors influencing its prediction accuracy, lacking an objective and comprehensive evaluation method. An improved approach combining Orthogonal Experiment Design (OED) and Principal Component Analysis (PCA) is employed to address these limitations. The evaluation method expands the noise metrics and provides a comprehensive assessment of the accuracy of numerical simulation for aerodynamic noise. The evaluation method is utilized to optimize and quantitatively analyze the impact of the refinement size of the core area on noise prediction for single-stage axial fans. Subsequently, the three metrics, namely Z1, Z2, and broadband noise Z3, are integrated using PCA to form a new integrated optimal metric Ztotal. The influence of different refinement sizes, particularly on Ztotal, is quantitatively examined. The findings reveal that the mesh size of the stator wake (D area) exhibits the most significant influence on noise

prediction accuracy, with a calculated weight of 81.3% on noise accuracy. Furthermore, a comprehensive investigation is conducted on the influence of turbulence models and the wall Y+ value on aerodynamic noise. Detached-Eddy Simulation (DES) and Large Eddy Simulation (LES) demonstrate effective capabilities in simulating both upstream and downstream turbulent flow characteristics of the stator, enabling accurate prediction of broadband noise. This study presents a set of numerical simulation schemes that achieve precise prediction of turbomachinery aerodynamic noise.

Keywords：Single-stage axial fan; Aerodynamic noise; Evaluation method; Numerical simulation; Broadband noise; Noise accuracy

1. Introduction

The issue of aerodynamic noise has gained prominence with the progression towards higher power and enhanced performance in fan and other turbomachinery products. It encompasses various critical aspects, including human well-being, communication, as well as the concealment of military equipment and the potential for acoustic fatigue damage to

machinery [1-4]. The aeroacoustic design of the fan, similar to its structural and aerodynamic designs, assumes a crucial and indispensable role in the overall design process. A comprehensive exploration of the mechanisms and characteristics of fan aerodynamic noise serves as the foundational basis for its aeroacoustic design.

The most accurate prediction of fan aerodynamic noise, in theory, necessitates the utilization of Direct Numerical Simulation (DNS), particularly for capturing the broadband noise generated by random pulsating forces. However, DNS requires substantial computing resources, rendering its practical application in engineering contexts unfeasible [5-7]. As an alternative approach suitable for practical applications, the hybrid method decouples the interaction of sound and flow, dividing the sound source generation and propagation into distinct processes. The methodology strikes a balance between accuracy and computational resources, leading to its widespread adoption [8-11]. The precise characterization of the vortex structure within the fan constitutes the primary focus of numerical investigations on broadband noise, originating from that broadband noise arises from random pressure fluctuations caused

by unsteady flow. In this regard, the combination of Large Eddy Simulation (LES) and Computational Aero-Acoustics (CAA) emerges as the preferred approach among researchers, as LES can effectively capture the eddy structures in the flow [12-15]. Tomimatsu et al. [16] conducted LES calculations for a single-stage jet fan employing a high-performance computer, revealing that finer mesh resolutions led to more accurate blade surface pressure distributions compared to coarser meshes. Wasala et al. [17] extracted the unsteady pressure sound source on the surface of an axial fan blade using LES, with experimental results demonstrating good agreement with numerical predictions based on the Ffowcs Williams-Hawkings (FW-H) equation. However, the LES/CAA numerical method for predicting fan broadband noise necessitates substantial computational resources when dealing with a large number of fan blades. Arroyo et al. [13] simplified the number of rotor and stator blades in a single-stage fan to 2:3 and employed 75 million elements to conduct LES investigations, enabling the accurate depiction of boundary layer separation and transition flow phenomena on the stator surface. Similarly, Lewis et al. [18] reduced the number of rotor and stator blades in an axial flow fan to 1:2 and

employed 95 million elements to demonstrate that boundary layer separation flow produces a significant sound source on the suction surface of the stator.

The wide application of LES in engineering practice is currently challenging since strict requirements on mesh size and time step for the flow field analysis. The analysis of the flow layer near the wall using wall-resolved LES is associated with a high computational cost. When dealing with flows with Reynolds numbers exceeding 10^5, resolving the wall layer, which constitutes less than 10% of the computational domain, requires more than 90% of the mesh points [5]. The Detached-Eddy Simulation (DES) has been proposed by scholars to alleviate the computational resource demands of LES, which combines Reynolds-averaged Navier-Stokes (RANS) and LES, resulting in significant reduction in computational cost [19-22]. RANS is employed to treat the wall layer near the solid wall to handle the region where turbulence scale is smaller than the maximum mesh size. The LES model is adopted to solve the flow in the turbulent core region, dominated by large-scale unsteady turbulence, where the turbulence length scale exceeds the mesh size. Therefore,

DES/CAA emerges as an optimal solution for accurate prediction of fan aerodynamic noise within reasonable computing resources. It enables the accurate capture of large-scale eddies in the core area of turbulent flow through LES, while utilizing RANS to reduce computational cost near the wall, thus achieving a suitable balance between prediction accuracy and computing cost [23-27].

Furthermore, the broadband noise characteristics of fans have been investigated by several researchers using the Unsteady Reynolds-Averaged Navier-Stokes (URANS) approach. The URANS model was utilized by Wohlbrandt et al. [28] to incorporate the cyclostationary features of the rotor wake and synthesize the turbulent flow field of the stationary blade. The rotor-stator interaction noise was successfully predicted by considering the period of turbulence, and achieved good agreement with experimental data. Park et al. [29] explored the broadband noise of the fan using the RANS turbulence model and identified two distinct broadband noise sources associated with the shroud. Additionally, Kim et al. [30] employed URANS and Large Eddy Simulation (LES) to predict the noise characteristics of axial fans individually. The results demonstrated that

both URANS and LES provided accurate predictions of the aerodynamic noise of fans, with a difference of less than 5%. Notably, LES exhibited advantages in predicting broadband noise.

However, uncertainties still exist in the prediction of turbomachinery aerodynamic noise, particularly broadband noise, when employing Computational Fluid Dynamics (CFD) combined with CAA. Deviations in noise prediction results can arise from changes in certain key parameters, yet literature on this topic is scarce. The influence of four different URANS schemes on fan broadband noise prediction was investigated by Grace et al. [31, 32] and Maunus et al. [33]. These studies considered various factors such as turbulence models, mesh topologies, and tip clearances. Significant differences were observed in the radial distribution of background turbulence intensity, leading to variations in broadband noise of up to 5 dB at low frequencies. Another study conducted by Jaron et al. [34] focused on the Source Diagnostic Test (SDT) fan. The impact of four different turbulence models on broadband noise was examined under approach conditions by employing the same mesh and solution settings. The results indicated that different turbulence models could influence broadband noise

by up to 2 dB. Guerin et al. [35] and Kissner et al. [36] from the German Aerospace Center (DLR) conducted a comprehensive and detailed investigation of the URANS/CAA scheme. 22 numerical schemes from 6 solvers, encompassing 4 tip clearances, 6 turbulence models, and 12 acoustic models were compared. The results emphasized that the selection of turbulence model and acoustic model had the most significant impact on fan noise, particularly the latter's profound influence on low-frequency broadband noise.

A unified and comprehensive understanding of its prediction accuracy has not yet been established although a considerable number of numerical studies have been conducted on fan aerodynamic noise. Previous research has predominantly relied on subjective evaluations by researchers themselves to assess the accuracy of aerodynamic noise prediction, lacking quantitative analysis of key factors. Consequently, an objective and comprehensive evaluation method remains absent. Therefore, it is imperative to thoroughly analyze the influence of specific key parameters on the prediction accuracy of fan aerodynamic noise and quantitatively assess the extent of their impact from an engineering application standpoint.

The analysis will ultimately facilitate the development of an objective and comprehensive aerodynamic noise prediction and evaluation method, thereby providing technical guidance for numerous practical applications involving aerodynamic noise prediction.

In this paper, a comprehensive evaluation method is formed by employing an improvement that combines Orthogonal Experiment Design (OED) and Principal Component Analysis (PCA). The evaluation method is applied to optimize and quantitatively analyze the impact of the refinement size of the core area on noise prediction for single-stage axial fans. Subsequently, PCA is used to integrate the three metrics, namely Total Sound Pressure (TSP) Z1, Typical Single-Tone (TST) Z2, and broadband noise Z3, resulting in the formation of a new integrated optimal metric Ztotal. The quantitative examination focuses on the influence of different refinement sizes, particularly on Ztotal. Additionally, a comprehensive investigation is conducted to analyze the influence of turbulence models and the wall Y+ value on aerodynamic noise, eventually developing a set of numerical simulation schemes that effectively achieve precise prediction of turbomachinery aerodynamic noise.

2. Evaluation model

The evaluation method for assessing the impact on the prediction accuracy of aerodynamic noise is based on a combined approach of OED and PCA. The traditional OED serves as the foundation, while PCA is introduced to further analyze and process the results of the OED, thereby obtaining a comprehensive evaluation. Detailed information is provided regarding the extent of influence and sensitivity classification of each factor on the prediction accuracy of aerodynamic noise. The OED is employed initially to reduce the number of numerical simulation schemes, and partial simulation results are utilized to assess the overall simulation situation. The average value of the optimization metrics is then computed across various factors and multiple levels. Subsequently, PCA is implemented to conduct optimal synthesis and dimensionality reduction on the average value of the optimization metrics, leading to the quantification of the influence degree between the new integrated optimal metric and multiple factors.

2.1. Orthogonal experiment design

The fundamental concept of the OED is to employ an orthogonal table to determine the multi-factor experiment. The OED is conducted to obtain experimental results, and subsequently, the results of these experiments are analyzed to select the optimal combination of multi-factor levels [37-40].

The multi-factor level orthogonal combination scheme exhibits a spatial distribution resembling cube nodes. Figure 1 depicts a schematic diagram illustrating a comprehensive experiment and the OED for a 3-factor, 3-level scenario, with each node representing a test. The comprehensive experiment entails conducting tests at all cube nodes, enabling the acquisition of the most comprehensive optimization metrics for each factor. However, this approach incurs significant costs, as shown in Figure 1(a). Alternatively, the resulting vectors formed by their numbers on the three factors are orthogonal by selecting only specific nodes, constituting the OED, as depicted in Figure 1(b). The 9 selected test points are distributed orthogonally within the cube, and conducting tests on these 9 combination schemes reasonably represents the comprehensive

experiment. The optimal multi-factor level combination scheme can be determined by analyzing the results of the OED.

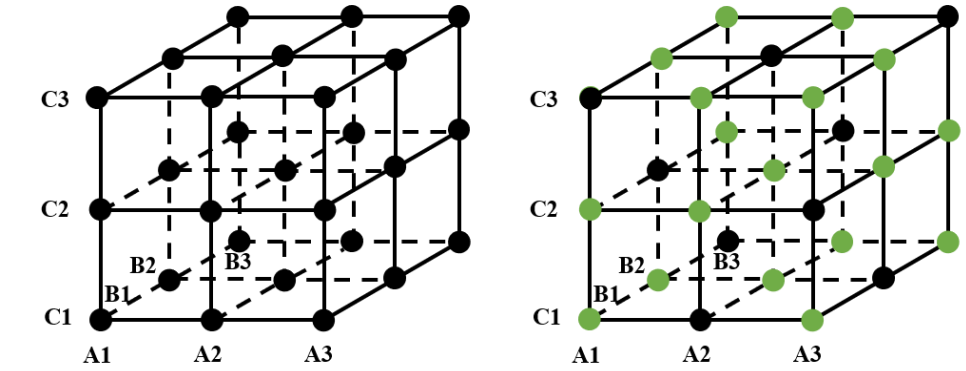

(a) The comprehensive experiment (b) The OED

Figure 1. Schematic diagram of comprehensive experiment and OED.

The orthogonality of the table is guaranteed by ensuring that the vectors formed by the numbers corresponding to multiple factors for each scheme are orthogonal. The numbers in the orthogonal table with 3 factors and 3 levels correspond to the point coordinates in Figure 1(b). Orthogonal tables possess not only orthogonality but also representation and comprehensiveness. The former guarantees that the OED is evenly distributed within the comprehensive experimental scheme, thus being highly representative. The latter indicates that when comparing different levels of a particular factor, the effects of other factors are balanced out, allowing for a comprehensive comparison of the influence of different

levels of each experimental factor on the optimization metrics. Commonly used orthogonal tables include $L_9(3^3)$, $L_9(3^4)$, $L_{16}(4^5)$, and so on.

The OED is commonly employed for the design of optimization schemes. The optimization metrics are subjected to processing to incorporate the OED into the investigation of aerodynamic noise prediction accuracy in this paper. The noise spectrum predicted by simulation is utilized as the optimization metrics, with the aim of minimizing the gap between the predicted noise spectrum and the experimental data. A smaller value indicates higher accuracy in noise prediction, ultimately leading to the identification of the numerical simulation scheme with the smallest noise prediction error. Moreover, three optimization metrics are expanded to formulate a comprehensive evaluation method for assessing the accuracy of aerodynamic noise prediction.

2.2. Principal component analysis

The dimensionality of high-dimensional space problems can be reduced through the utilization of PCA, thereby simplifying the problem and enhancing its intuitiveness. The resulting metrics from dimensionality

reduction are independent of each other, yet they retain a significant portion of the original high-dimensional space information. PCA serves as an effective approach to extract the principal features that encapsulate the majority of the information, enabling the identification of key components within the system and facilitating the comprehension of the principal structure during the analysis of intricate problems. PCA is known by different names in various fields, including Proper Orthogonal Decomposition (POD), Hotelling analysis, empirical component analysis, empirical eigenfunction decomposition, and others [41-44].

The input for PCA consists of the original matrix data, where there are m variables and each variable consists of n samples, and the i-th sample corresponding to the j-th variable is x_{ij}. The matrix $X_{n\times m}$ has n rows and m columns, representing the number of samples and variables, respectively. Its formulation is given by

$$X=\left\{x_1\left(x,t_1\right),x_2\left(x,t_2\right),x_3\left(x,t_3\right),\cdots x_m\left(x,t_m\right)\right\} \tag{1}$$

where x_i is the i-th variable with n samples. It is first necessary to standardize the data to scale the data to a specific range to facilitate the comparison and evaluation of the data since the units of the data are

inconsistent. The common standard deviation normalization method has

$$\tilde{x}_{ij} = \frac{x_{ij} - \overline{x}_j}{s_i}, (i = 1, 2, \cdots, n; j = 1, 2, \cdots, m) \tag{2}$$

$$\overline{x}_j = \frac{\sum_{i=1}^{m} x_{ij}}{n}, (j = 1, 2, \cdots, m) \tag{3}$$

$$s_j = \sqrt{\frac{\sum_{i=1}^{m} \left(x_{ij} - \overline{x}_j \right)^2}{m-1}}, (j = 1, 2, \cdots, m) \tag{4}$$

where $\overline{x}_j$ and s_j are the mean and standard deviation of the m-th sample, respectively. The standardized data conforms to the normal distribution, that is, the mean is 0 and the variance is 1.

The goal of PCA is to find the optimal basis vectors that can represent the given data, that is, to find the vector that can represent X optimally. The solution to this problem [45] can be implemented by finding the following eigenvectors and eigenvalues

$$RU_j = \lambda_j U_j \tag{5}$$

Where $R = \frac{X^T X}{n-1}$ is a square matrix of size $m \times m$, and $U_j = (u_{1j}, u_{2j}, u_{3j}, \cdots, u_{nj})^T$ and λ_j represent eigenvectors and eigenvalues, respectively, u_{nj} represents the n-th component of the j-th eigenvector. The feature vectors can be linearly combined into n new evaluation

functions in the new coordinate space

$$\begin{cases} y_1 = u_{11}\tilde{x}_1 + u_{21}\tilde{x}_2 + \cdots + u_{n1}\tilde{x}_n, \\ y_2 = u_{12}\tilde{x}_1 + u_{22}\tilde{x}_2 + \cdots + u_{n2}\tilde{x}_n, \\ \vdots \\ y_n = u_{1n}\tilde{x}_1 + u_{2n}\tilde{x}_2 + \cdots + u_{nn}\tilde{x}_n. \end{cases} \tag{6}$$

Where y_1 is the first principal component, y_2 is the second principal component, … , and y_n is the n-th principal component. In addition, the ratio of the eigenvalues λ_j to the sum of all eigenvalues represents the contribution of the j-th principal component y_j , so the contribution of the j-th principal component y_j and the cumulative contribution of the first r principal components (y_1, y_2,… , y_r) are respectively

$$b_j = \frac{\lambda_j}{\sum_{k=1}^{n}\lambda_k} (j = 1,2,\cdots,n), \tag{7}$$

$$B_r = \frac{\sum_{k=1}^{r}\lambda_k}{\sum_{k=1}^{n}\lambda_k} \quad (r,, n). \tag{8}$$

Where b_j and B_r are the contribution of the j -th principal component y_j and the cumulative contribution of the first r principal components, respectively. It indicates that the first r principal components contain enough original information when the cumulative contribution of them reaches 85%, which can be used to analyze the characteristics of the

entire model. At this time, the selected principal components can be adopted to weight to obtain the final comprehensive evaluation function Y_Z

$$Y_z = \sum_{j=1}^{r} \frac{\lambda_j y_j}{\sum_{k=1}^{r} \lambda_k} \tag{9}$$

The quantitative influence of each factor on the prediction accuracy of aerodynamic noise is determined through the utilization of the final comprehensive evaluation function, and the ranking of the prediction accuracy of aerodynamic noise is accomplished by utilizing the sensitivity results.

2.3. Evaluation process

The evaluation method employed in this paper is enhanced and refined by incorporating and introducing the methods of OED and PCA into the field of numerical simulation for aerodynamic noise prediction accuracy. The optimization metrics are expanded for noise prediction, and the comprehensive evaluation method for numerical prediction accuracy of noise is subsequently developed, as depicted in Figure 2.

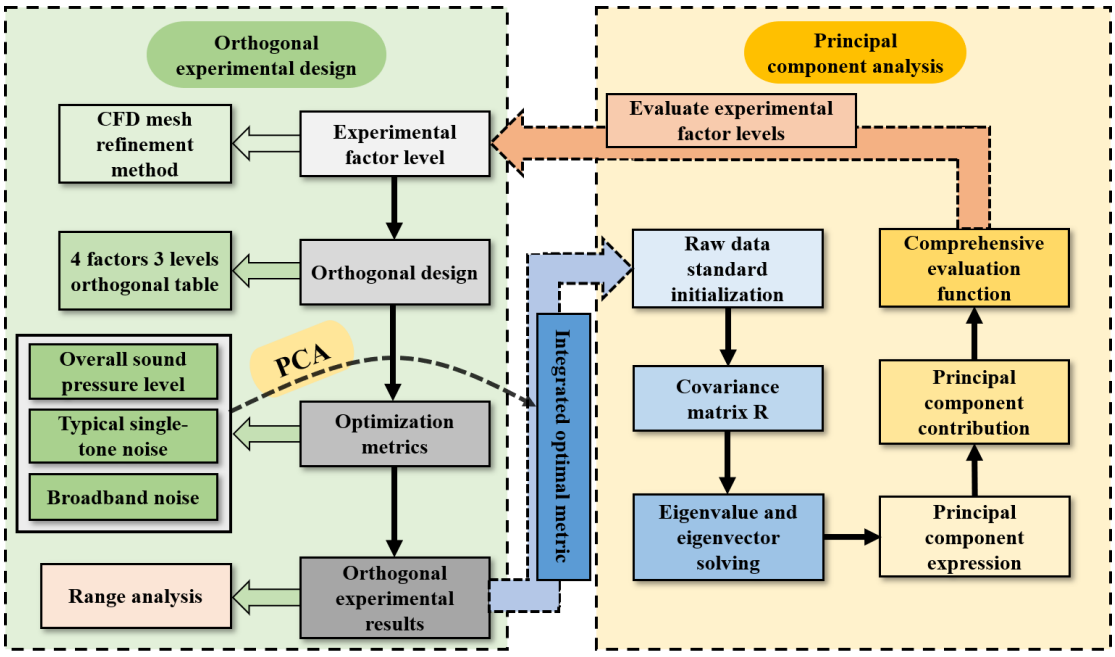

Figure 2. Flowchart of the evaluation method of OED combined with PCA.

The investigated single-stage axial flow fan in this paper comprises 9 rotors and 11 stators, necessitating an accurate prediction of fan broadband noise. It is necessary to carry out refined CFD simulation of the fan, which demands substantial computing resources. The CFD commercial code employed in this study is Star-CCM+, which utilizes polyhedral mesh technology to diminish mesh quantities and computational workloads. Consequently, the experimental factors and levels should be limited to minimize computational costs, even if the OED can substitute some experiments for the comprehensive one. The OED includes only four factors related to mesh refinement for selecting the optimal mesh

refinement scheme, followed by an analysis of the influence of other factors such as wall Y+ value and turbulence models on the prediction accuracy of aerodynamic noise.

The accuracy of aerodynamic noise prediction for a single-stage axial flow fan is comprehensively evaluated by synthesizing a new integrated optimal metric using the PCA method based on the aforementioned three optimization metrics. The average matrix of the integrated optimal metric serves as the input for PCA, which is first standardized. Subsequently, the covariance matrix R is constructed, and the eigenvalues and eigenvectors of matrix R are sequentially calculated. The expression of the principal component is derived, and the contribution of each principal component is analyzed. Further analysis of the impact of different refinement methods on noise prediction is facilitated by determining the comprehensive evaluation function. The degree of influence and sensitivity of the refinement method on the prediction accuracy of aerodynamic noise are quantitatively determined.

3. Evaluation model of mesh refinement method

3.1. Hybrid prediction method for the single-stage axial fan

The geometric structure configuration and numerical calculation domains of the single-stage axial fan are presented in Figure 3. The fan consists of four domains, namely the intake pipe, rotor, stator, and exhaust pipe. The lengths of the intake and exhaust pipes correspond to those of the fan test bench, ensuring the reflection of real flow distribution and promoting the stable development of inlet and outlet airflow. The intake pipe has a conical structure in its initial section to facilitate uniform and smooth airflow into the fan. The rotor is driven by a motor placed downstream of the stator, and the motor casing forms a solid wall (indicated by the brown marked surface in the figure). The CFD simulation also includes the modeling of the electrical connection path between the motor and the external frequency converter, represented by the box next to the motor (indicated by the green marked surface in the figure). Additionally, the motor is supported by the support in the round tube (indicated by the blue marked surface in the figure) to prevent motor

deformation caused by gravity. All motor-related accessories are accurately modeled to closely replicate the configuration of the actual test bench, minimizing numerical calculation errors arising from geometric disparities. Other parameters for the single-stage fan are shown in Table 1.

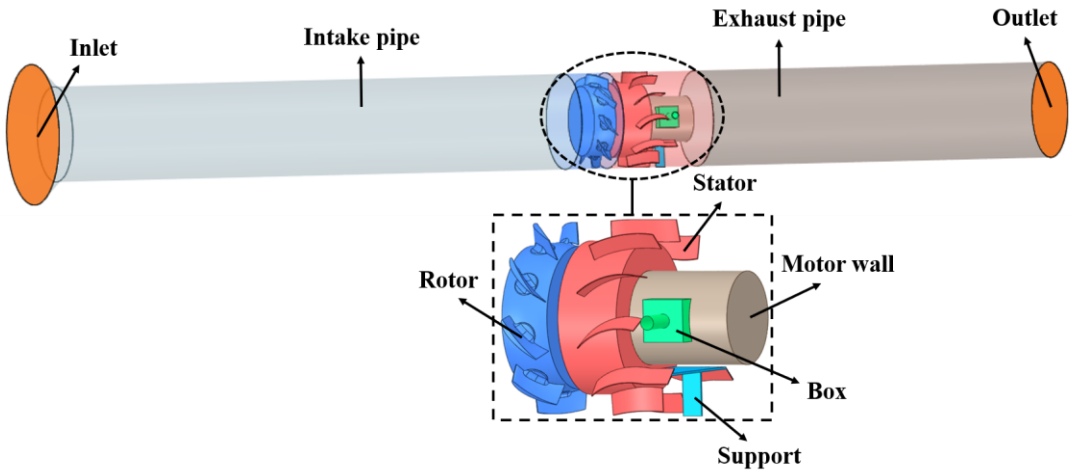

Figure 3. The configuration of the single-stage axial fan.

In practical applications, the Finite Element Method (FEM) is particularly suitable for sound prediction under complex structures, which can be fully modeled to analyze the reflection and scattering of sound. For turbomachineries, the single-tone noise corresponding to the BPF is the most significant [46] and the first three orders of the BPF should be considered. The BPF and its harmonic frequencies are given by equation (10)

$$f = \frac{nBi}{60}, \tag{10}$$

where n is the rotor speed, B is the number of rotor blades, i is the harmonic order, and f is the blade passing frequency. The third order BPF for the compressor studied here is 990 Hz and the maximum frequency of interest for this paper was, therefore, set equal to 3000 Hz. There have been many studies on the size of the acoustic grid required for noise calculation [47, 48], which have shown that it is often necessary to ensure that there are six elements within the wavelength of the highest frequency noise. The acoustic mesh contained ten elements within the wavelength of the highest frequency noise and a total number of 5.7 million elements were formed as shown in Figure 4. It is noteworthy that the rotor region has been entirely modeled to emulate the dissipation of noise as it travels through the blade row to the upstream region, thereby enhancing the fidelity of noise propagation simulation to real-world conditions. Furthermore, the intake and exhaust ducts have undergone comprehensive modeling, encompassing the establishment of hemispherical-like propagation regions at their terminations and the imposition of non-reflective boundary

conditions on these hemispherical-like surfaces. Lastly, the tapered pipe at the terminus of the intake pipe and the 3mm-thick exhaust pipe have been meticulously incorporated into the model, as indicated within the blue circle in the figure, to precisely replicate the actual experimental environment.

The noise prediction process involves employing a combination of CFD and FEM, which separately calculate the flow field and sound field. Unsteady flow field calculations are conducted initially to obtain the aerodynamic noise source. Subsequently, predictions of far-field acoustic radiation are performed based on the sound source derived from the CFD calculations. The methodology incorporates Lighthill's theory in variational form to extract aerodynamic sound sources from the flow fields, before the FEM is applied to propagate the noise and predict the far-field acoustic radiation. For a comprehensive description of this method, please refer to our previous work [49].

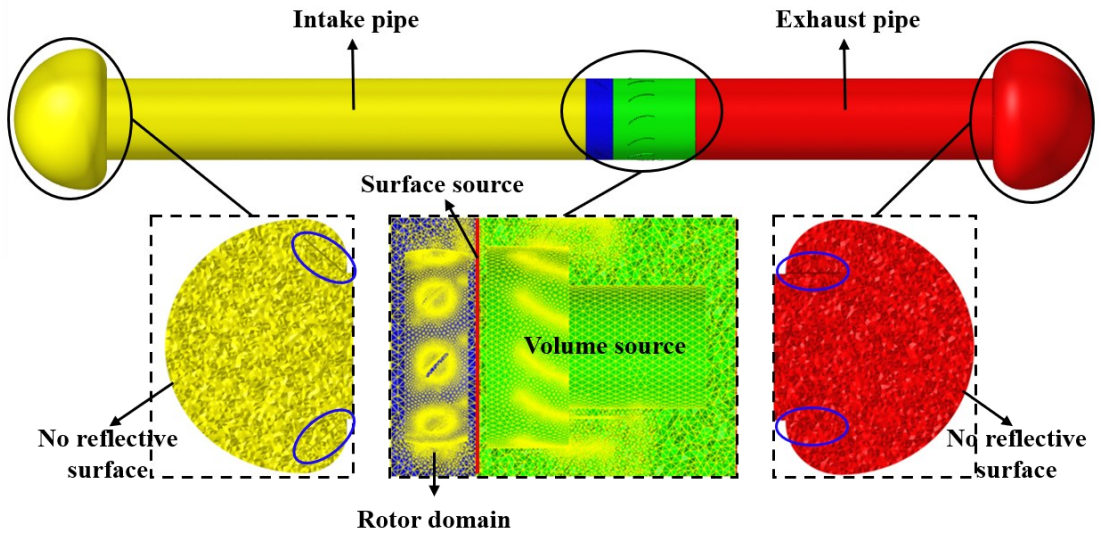

Figure 4. Acoustic mesh for CAA mode of the axial fan.

Table 1. Other parameter for the single-stage axial fan.

Rotating speed	2200 r/min
Installation angle	38 deg
Shroud diameter	460 mm
hub diameter	338 mm
Number of rotor blades	9
Number of stator blades	11
Tip clearance	5 mm

2.2. Determination of factors and levels

The prediction accuracy of aerodynamic noise in numerical simulations relies on the precise representation of the aerodynamic sound source in CFD, including the mesh, solution algorithm, turbulence model, as well as

acoustic model. Incorporating all these factors into the OED simultaneously incurs significant computational costs. It has been noted by Kissner that the impact of the mesh on broadband noise is negligible, but only when a fine mesh is generated by an experienced turbomachinery specialist [36]. However, the refinement of the mesh in the core flow region remains a critical factor that influences the accuracy of aerodynamic noise prediction, particularly for broadband noise. It is challenging in reality for researchers who are new to the field of turbomachinery to determine when the mesh is adequately refined. Therefore, conducting specific quantitative research on the influence of mesh refinement on aerodynamic noise is of great significance.

The single-stage axial flow fan under investigation comprises two core CFD domains: the rotor and the stator. Four areas requiring mesh refinement are identified as a result: (A) the entire rotor, (B) the entire stator, (C) the rotor wake, and (D) the stator wake. These four mesh refinement areas are orthogonally designed to determine the most suitable refinement method, aiming to reduce the number of elements while improving the accuracy of noise prediction. Figure 5 depicts the refinement areas of the

impeller region, which include the aforementioned four areas as well as an additional refinement area extending from the rotor-stator interface to a distance of 40 mm away from the stator's leading edge. It is widely recognized that the Rotor-Stator Interaction (RSI) is the primary mechanism governing the aerodynamic noise of a single-stage fan, encompassing both single-tone noise and broadband noise. The yellow refinement area's mesh size matches that of the rotor wake, ensuring that captured rotor wakes propagate smoothly to the stator's leading edge and enabling a refined simulation of the RSI effect. Moreover, the refined region near the rotor surface accounts for complex flow phenomena such as separation flow, facilitated by the dilation angle (40 degrees) of the rotor wake shown in the figure.

Other possible influencing factors need to be kept in line in order to study the effect of mesh refinement on noise prediction first. The Shear Stress Transport (SST) turbulence model is given primary consideration based on numerous previous numerical simulation studies of turbomachinery [50, 51]. The SST model, a low Reynolds number model within the URANS framework, necessitates specific adjustments for the

first layer thickness near the wall in core regions such as the rotor and stator surfaces. The first layer thickness is set to 0.01mm, comprising 13 boundary layers to accurately simulate the velocity gradient and separated flow near the wall. The configuration ensures that the velocity distribution of viscous bottom is directly solved by mesh nodes rather than relying on approximate wall functions. The SST turbulence model imposes stringent requirements on the wall-adjacent mesh, aiming to maintain a wall Y+ value of less than 5 [52, 53]. Figure 6 illustrates the distribution of Y+ values on the blade surfaces, demonstrating that the maximum Y+ does not exceed 1.5, which is deemed acceptable.

It is crucial to establish reasonable factor levels to ensure the effectiveness of the OED and accurately predict the fan noise within the selected factor range. The noise data obtained by separately refining the core domains and the areas of blade wake are compared with the experimental results in this paper, as illustrated in Figure 7, to determine an appropriate factor level. The initial element size of the numerical domains is set at 6 mm, with subsequent refinement of the mesh size in the core domains to 2.5 mm and in the wake areas to 1.5 mm. The number of

elements in the domain with a size of 2.5 mm reaches 23 million, while in the wake area with a size of 1.5 mm, it reaches 18 million. The refined results exhibit a significant improvement in their proximity to the experimental values, particularly at the single-tone frequencies, encompassing the Blade Passing Frequency (BPF) and its harmonics. The unrefined mesh underestimates the results above 500 Hz in terms of broadband noise, whereas the refined grid yields better predictions for broadband noise. Therefore, the minimum element size for refinement in the core domains is determined as 2.5 mm, while for the wake areas, it is set at 1.5 mm. The maximum element sizes for the core domains and wake areas are chosen as 7.5 mm (slightly larger than the initial mesh size depicted in the figure) and 2.5 mm (ensuring that the element size of the wake areas remains smaller than that of the core domains), respectively. Three levels are considered for each of the four factors, and the middle refinement size is determined as the average value between the maximum and minimum sizes. These values are presented in Table 2. The specific design scheme aligns with the four-factor, three-level orthogonal table mentioned in Section 2.1, as demonstrated in Table 3.

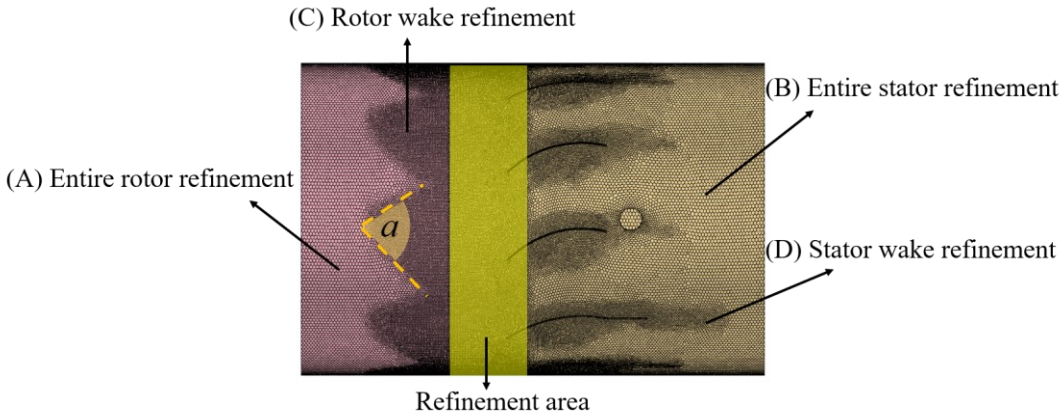

Figure 5. The configuration of the single-stage axial fan.

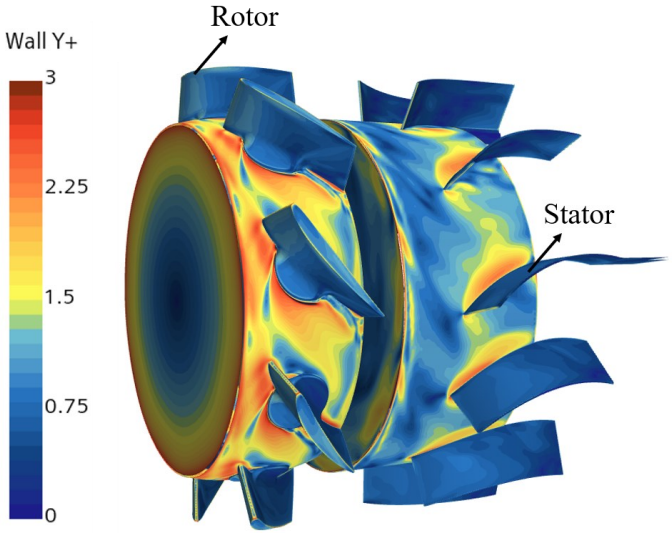

Figure 6. The Y plus distribution of the blades surfaces.

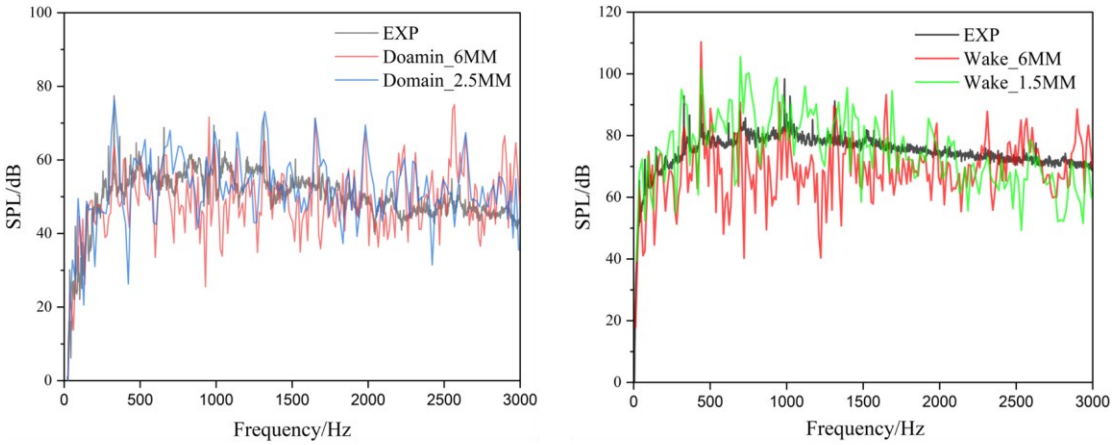

(a) Comparison of noise spectra between refined and unrefined core domains

(b) Comparison of noise spectra between refined and unrefined wake areas

Figure 7. Effects of core domains and wake areas refinement on noise prediction results.

Table 2. Determination of experimental factors and levels.

Levels	Factors			
	Size of A /mm	Size of B /mm	Size of C /mm	Size of D /mm
1	7.5	7.5	2.5	2.5
2	5	5	2	2
3	2.5	2.5	1.5	1.5

Table 3. Specific design scheme for the four-factor, three-level orthogonal table

Number	Size of A /mm	Size of B /mm	Size of C /mm	Size of D /mm
1	A1 (7.5)	B1 (7.5)	C1 (2.5)	D1 (2.5)
2	A1	B2 (5)	C3 (1.5)	D2 (2)
3	A1	B3 (2.5)	C2 (2)	D3 (1.5)
4	A2 (5)	B1	C3	D3

Number	Size of A /mm	Size of B /mm	Size of C /mm	Size of D /mm
5	A2	B2	C2	D1
6	A2	B3	C1	D2
7	A3 (2.5)	B1	C2	D2
8	A3	B2	C1	D3
9	A3	B3	C3	D1

2.3. The optimization metrics

The application of OED is employed to determine the necessary refinement area and size to effectively capture the random pressure fluctuations induced by vortex structures, ultimately enabling accurate prediction of the axial fan's aerodynamic noise. Furthermore, the approach involves optimization design, which necessitates the consideration of appropriate optimization metrics. The optimization metrics are defined as the discrepancies between the numerically predicted noise and the experimental measurements in this paper. Specifically, the accuracy evaluation of fan aerodynamic noise is predominantly focused on three aspects: (i) the gap in Total Sound Pressure (TSP) level, denoted as Z1, (ii) the gap in Typical Single-Tone (TST) noise, denoted as Z2, and (iii) the

gap in broadband noise, denoted as Z3.

The optimization metric Z1 represents the discrepancy between experimental and numerical data. A smaller difference indicates higher accuracy in the numerical simulation. For the optimization metric Z2, which pertains to the TST noise characteristics of the fan, the prominence of the first four-order BPF harmonics is evident from the experimentally measured noise (Figure 8). In contrast, the peaks of BPF harmonics beyond the fifth order are not as pronounced. The optimization metric Z2 is calculated as the average difference between the values of the first four-order BPF harmonics obtained from numerical calculations and the corresponding experimental results. The weights assigned to the BPF harmonics of different orders are equal. The optimization metric Z3 addresses the discrepancy in broadband noise within the frequency range of interest (up to 3000 Hz due to the low speed). It involves calculating the absolute area between the experimental and numerical spectra using an integral method, as depicted by the green region in Figure 9. The integration of the discrepancy area is influenced by the frequency resolution employed in the simulation and experiment. The noise spectrum

obtained from the experiment maintains a resolution of 1 Hz, while a fixed resolution of 18.3 Hz is maintained in the simulation during the implementation of the OED to mitigate the errors caused by data resolution differences. It is important to note that the absolute area corresponding to the broadband noise is standardized by dividing it by 3000 to ensure its magnitude is consistent with the previous two optimization metrics. Finally, the optimization of the aforementioned evaluation metrics involves quantitative analysis of the data, facilitating subsequent data analysis and optimization processes.

Z1 is compared with experimental data at three specific points, and the average of these three differences is used as the final quantitative analysis data to minimize errors. In the case of Z2 for the axial fan, the total of 12 data points is compared and averaged to obtain the optimized metrics. Similarly, spectral data from three points are integrated to calculate the absolute area for the evaluation of broadband noise Z3, followed by averaging. These measurement points are positioned at a distance of one meter from the entrance plane and are distributed evenly at 45-degree intervals around the circumference, as depicted in Figure 10.

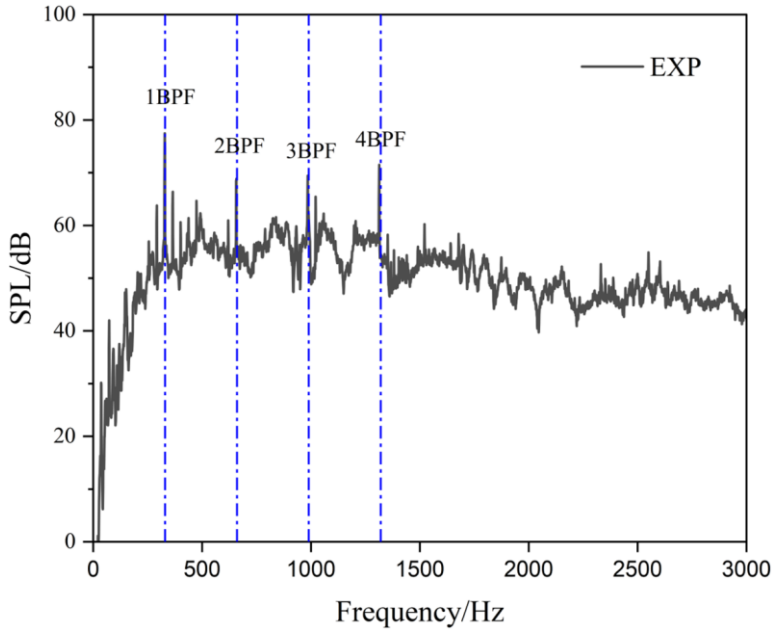

Figure 8. TST noise Z2 measured by experiment of axial flow fan.

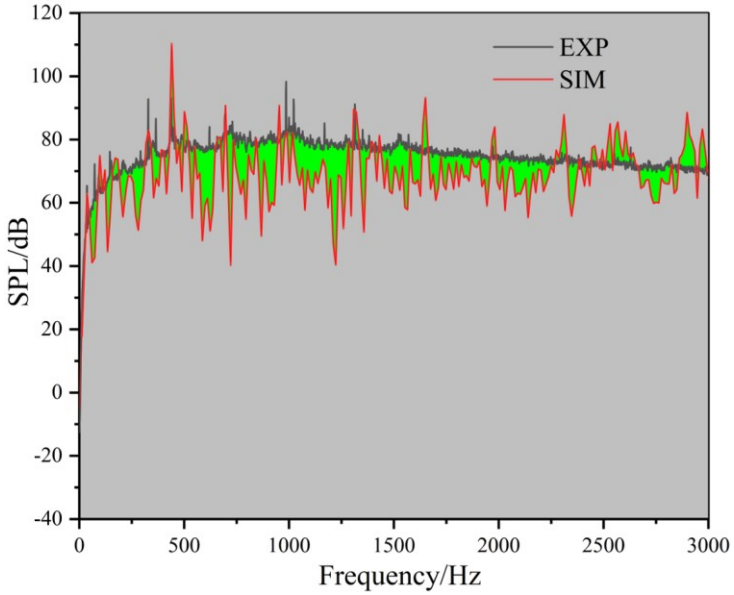

Figure 9. The absolute area of broadband noise Z3 gap of axial flow fan.

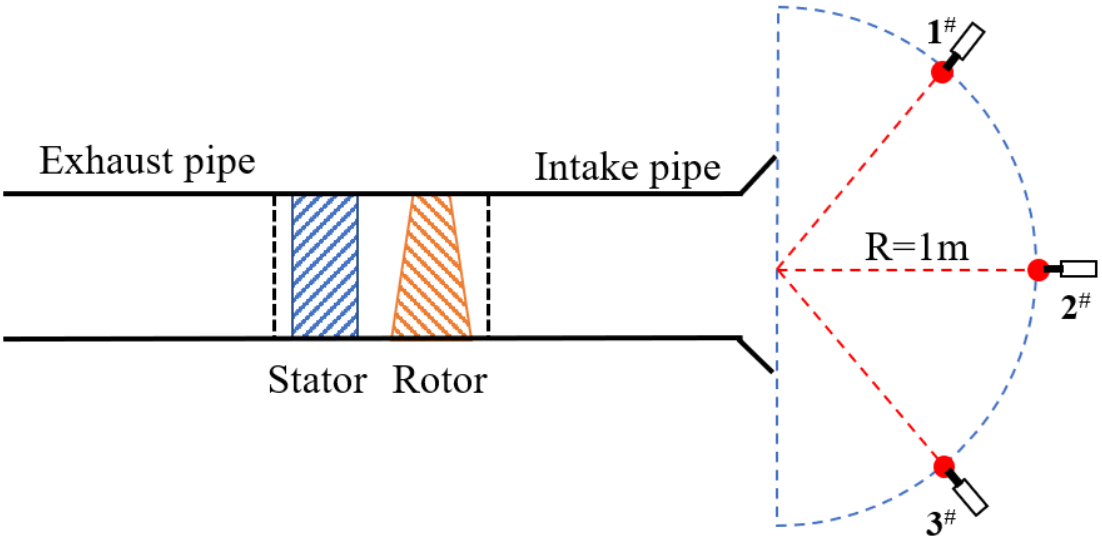

Figure 10. Distribution of noise measurement points for axial fans.

2.4. Experimental configuration

The axial fan experiment is conducted within a fan aerodynamic noise test bench, wherein air is drawn into the intake duct, subjected to compression by the axial fan for performing work, and subsequently expelled through the exhaust duct. The intake duct comprises distinct sections, namely the horn-shaped inlet section, the measurement section, and the intake stabilization section. The horn-shaped inlet is designed to facilitate the ingress of airflow into the system with optimal smoothness. Within the measurement section, flow and pressure parameters of the fan are quantified, while the intake stabilization section ensures a consistent

and steady intake of air. The exhaust duct is primarily composed of the exhaust stabilization section, the pressure measurement section, and a flow regulating cone, which is contribute to the regulation of the fan's operating conditions. The fan is driven by a three-phase AC motor situated at the rear of the stator, directly coupled to the rotor. A visual representation of the physical fan experimental setup is provided in Figure 11.

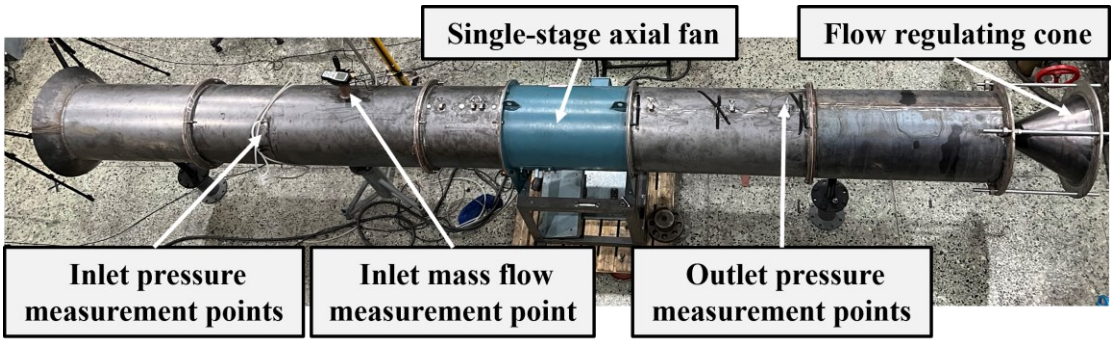

Figure 11. The test bench of single-stage axial fan.

To validate the precision of the simulation, three measurement points are arranged at the horn-shaped inlet, positioned at a distance of 1 meter from the inlet's center, as visually represented in Figure 12. Noise data is collected by the B&K2671 acoustic microphones meticulously placed at their respective positions along the entrance. The data acquisition card employed in this process is the BK Company's Model 3050. An acquisition time of 30 seconds is utilized to guarantee the acquisition of experimental data with a high degree of resolution.

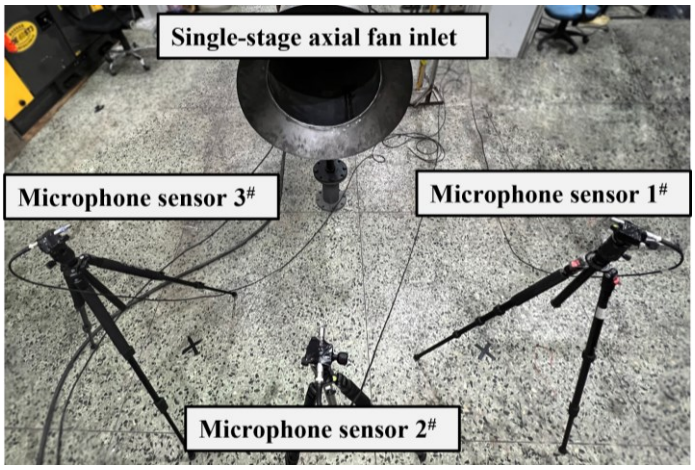

Figure 12. Position of inlet measuring points.

4. Results and discussion

4.1. Range analysis

The numerical simulation results of the OED for single-stage axial flow fans using different mesh refinement methods are presented in Table 4. The simulations are conducted with an installation angle of 38 degrees, a speed of 2200 rpm, and the valve fully opened. The OED employed a range of 9 refinement strategies, resulting in a variation in the number of elements from 8 to 19 million. Three optimization metrics obtained from the simulations are processed according to the methodology outlined in Section 2.3.

The average values of three optimization metrics are calculated based

on the findings presented in Table 4, and further analysis is performed to determine the range analysis. The results are illustrated in Table 5, where k1, k2, and k3 denote the average values of optimization metrics for a particular factor at levels 1, 2, and 3, respectively. The extreme difference R signifies the discrepancy between the maximum and minimum values of the average values of optimization metrics for the same factor. A larger value of R indicates a more pronounced influence of the factor on the optimization metrics.

Table 4. The results of OED

Number	Mesh number/million	TSP Z1/dB	TST Z2/dB	Z3/dB
1	8.36	1.50	4.20	10.38
2	14.17	6.33	6.03	9.82
3	15.86	3.39	7.03	11.34
4	16.11	3.90	6.28	10.30
5	10.22	1.52	4.83	10.34
6	12.78	3.55	6.83	9.30
7	12.27	2.85	5.63	10.23
8	13.84	2.95	5.41	9.68
9	19.01	0.73	4.04	9.56

It is evident that the size of domain D exerts a highly dominant impact among the first two optimization metrics, as indicated by its largest

variance in both TSP and TST. The size of domain A emerges as the second influential factor, significantly affecting TSP and TST. Conversely, the sizes of domains C and D exhibit minimal influence on the first two optimization metrics. However, the size of domain C displays the most significant influence in terms of the accuracy of broadband noise prediction, followed by the sizes of domains A and D, while the size of domain B exhibits the least impact on broadband noise. Notably, the extreme difference R associated with different factors on broadband noise is the smallest, indicating that achieving improved results in broadband noise prediction often necessitates simultaneous refinement of multiple areas.

Table 5. Range analysis table for OED

Optimization metrics	average value	Factors			
		Size of A	Size of B	Size of C	Size of D
TSP Z1 /dB	k_1	3.74	2.75	2.67	1.25
	k_2	2.99	3.60	2.59	4.24
	k_3	2.18	2.56	3.65	3.41
	R	1.56	1.04	1.06	2.99
TST Z2 /dB	k_1	5.75	5.37	5.48	4.36
	k_2	5.98	5.42	5.83	6.16
	k_3	5.03	5.97	5.45	6.24

	R	0.95	0.60	0.38	1.88
Z3 /dB	k_1	10.51	10.30	9.79	10.09
	k_2	9.98	9.95	10.64	9.78
	k_3	9.82	10.07	9.89	10.44
	R	0.69	0.35	0.85	0.66

Figure 13 illustrates the influence of different factors on the optimization metrics. Area A demonstrates a notable consistency across three optimization metrics, with higher noise prediction accuracy achieved through smaller sizes. On the other hand, reducing the size of region D results in larger deviations in TSP and TST predictions, potentially due to interference between the stator wake and downstream additional structures. The utilization of the SST turbulence model, a Reynolds-averaged model, can introduce bias when simulating complex phenomena like stator wakes and interference effects from downstream structures although finer meshes theoretically yield more accurate predictions. No clear rules emerge in the variation of each optimization metric with regions B and C. The optimal mesh refinement strategy can be selected to minimize the optimization metrics based on Figure 13. The recommended refinement strategies for

the three optimization schemes are as follows: CaseZ1 - A3B3C2D1, CaseZ2 - A3B1C3D1, and CaseZ3 - A3B2C3D2.

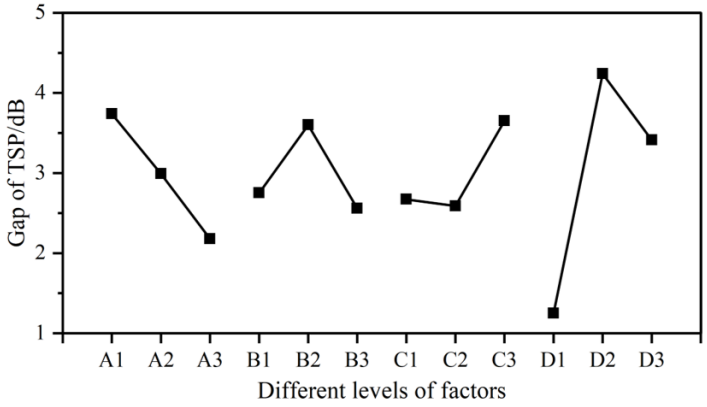

(a) The impact of different factors on TSP

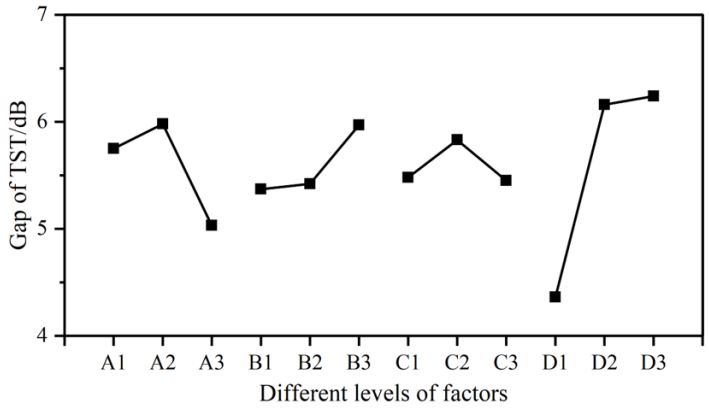

(b) The impact of different factors on TSP

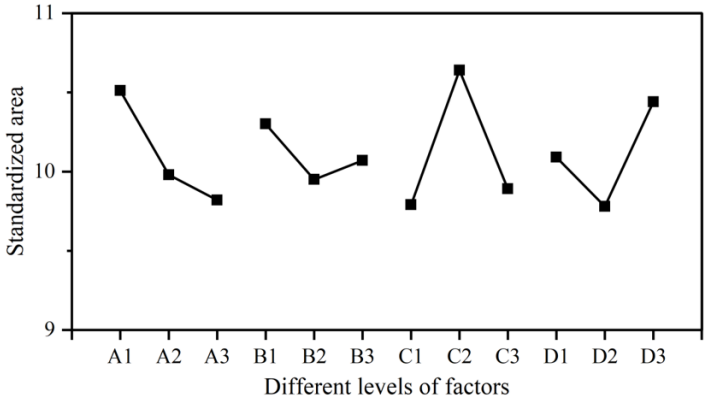

(c) The impact of different factors on broadband noise

Figure 13. Relationship between factors and optimization metrics.

4.2. Comprehensive evaluation

The three aforementioned optimization metrics are integrated into an evaluation system to achieve a comprehensive assessment of the accuracy of aerodynamic noise in single-stage axial flow fans. A crucial aspect is determining the contribution of each optimization metric to the integrated optimal metric. Notably, the proportion of Z3 in the integrated optimal metric should exceed that of Z1 and Z2 due to the inclusion of both broadband noise and single-tone noise differences in the area discrepancy of broadband noise Z3. It becomes necessary to construct a new integrated optimal metric, Ztotal, utilizing PCA to mitigate the impact of subjective factors on noise prediction accuracy.

Table 6 presents the data extraction efficiency of the integrated optimal metric Ztotal, utilizing Table 4 as input data for PCA. The principal component eigenvalues and their corresponding contribution fractions are depicted in Table 7. The data extraction rates for all three noise optimization metrics surpass 80%, indicating their suitability for PCA analysis. Three principal components are primarily extracted, accounting

for 57.744%, 33.942%, and 8.315% of the contribution fractions in the integrated optimal metric, respectively. The eigenvectors associated with these principal components are provided in Table 8. Consequently, the expressions for principal components 1 to 3 can be derived as

$$z_1 = 0.67799Z_1 + 0.71099Z_2 + 0.1866Z_3 \tag{11}$$

$$z_2 = -0.29942Z_1 + 0.03528Z_2 + 0.95347Z_3 \tag{12}$$

$$z_3 = 0.67132Z_1 - 0.70232Z_2 + 0.2368Z_3 \tag{13}$$

Table 6. Initial data extraction efficiency

Noise optimization metrics	Initial value	Extraction
Gap of TSP Z1	1.000	0.888
Gap of TST Z2	1.000	0.877
Gap of Z3	1.000	0.986

Table 7. Principal component eigenvalues and contribution fractions

Principal component	Eigenvalues	Contribution fractions /%	Cumulative contribution fraction /%
1	1.173	57.744	57.744
2	1.018	33.942	91.685
3	0.249	8.315	100.000

Table 8. Principal component eigenvectors

Principal component	TSP Z1	TST Z2	Z3
1	0.67799	-0.29942	0.67132
2	0.71099	0.03528	-0.70232
3	0.1866	0.95347	0.2368

The expression of the final integrated optimal metric Ztotal through equation (9) can be obtained as

$$Z_{total} = 0.345669Z_1 + 0.364102Z_2 + 0.45104Z_3 \quad (14)$$

The proportion of Z3 is the largest in the equation (14), reaching 45%, and the proportion of Z2 is slightly larger than that of Z1, which are 36% and 35% respectively. The proportion distribution obtained by PCA satisfies the law that the proportion of broadband noise Z3 is the largest, TST noise Z2 is second, and the TSP level Z1 is the smallest. In fact, the most eye-catching metric is Z3, because Z3 does not eliminate the difference of single-tone noise, which can best reflect the accuracy of predicting noise. The second is Z2, which is the main noise characteristic of rotating machinery under normal working conditions. The least important is the Z3, since the closeness of the experimental and simulated total sound pressure levels does not indicate that the spectrum of the

predicted noise is close to the experimentally measured value in the specified frequency range. This proportion allocation can form an integrated optimal metric to evaluate the accuracy of noise prediction from an objective perspective to the greatest extent.

The calculated results of the integrated optimal metric and range analysis are presented in Table 9. The noise prediction results are primarily influenced by the size of domain D, with domain A having the next highest impact. The ranking of the degree of influence on the noise prediction results is as follows: D>A>C>B. The optimal refinement strategy for the integrated optimal metric is determined to be CaseTtotal- A3B1C1D1.

Table 9. Range analysis table for the integrated optimal metric

Number	Size of A /mm	Size of B /mm	Size of C /mm	Size of D /mm	The integrated optimal metric
1	A1 (7.5)	B1 (7.5)	C1 (2.5)	D1 (2.5)	6.73
2	A1	B2 (5)	C3 (1.5)	D2 (2)	8.81
3	A1	B3 (2.5)	C2 (2)	D3 (1.5)	8.85
4	A2 (5)	B1	C3	D3	8.28
5	A2	B2	C2	D1	6.95
6	A2	B3	C1	D2	7.91
7	A3 (2.5)	B1	C2	D2	7.65

8	A3	B2	C1	D3	7.36
9	A3	B3	C3	D1	6.04
K1	8.13	7.55	7.33	6.57	
K2	7.71	7.71	7.81	8.12	
K3	7.01	7.60	7.71	8.16	
R	1.12	0.16	0.48	1.59	

The data input for PCA analysis consists of the average value of the integrated optimal metric for each factor, enabling further quantitative analysis of each factor's impact on the accuracy of noise prediction. The correlation coefficient diagram of the integrated optimal metric, denoted as Ztotal, is presented in Figure 14. Figure 15 provides the principal component eigenvalues and their corresponding contribution fractions. A majority of the correlation coefficients exceed the critical value of 0.33, indicating the suitability of the average value derived from the integrated optimal metric for PCA analysis. Two principal components are extracted, accounting for 91.51% and 8.49% of the variance in the integrated optimal metric, respectively. The eigenvectors associated with these principal components are calculated the expressions for principal components 1 and 2 are obtained as

$$y_1 = -0.46938x_1 + 0.04851x_2 + 0.2251x_3 + 0.85244x_4 \quad (15)$$

$$y_2 = 0.8566x_1 + 0.19921x_2 + 0.27673x_3 + 0.38726x_4 \quad (16)$$

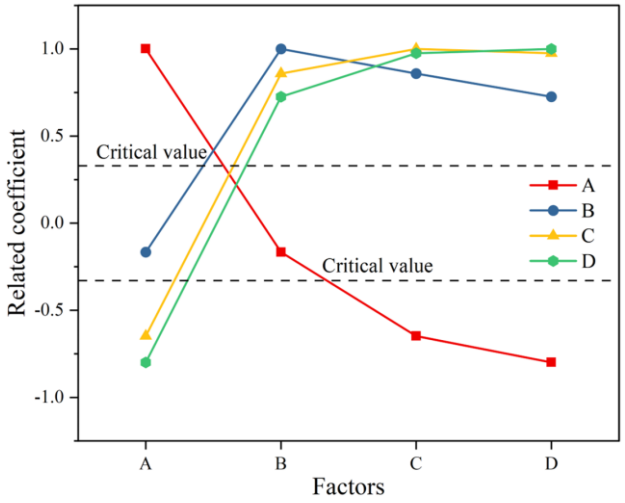

Figure 14. The distribution of correlation coefficients among different factors.

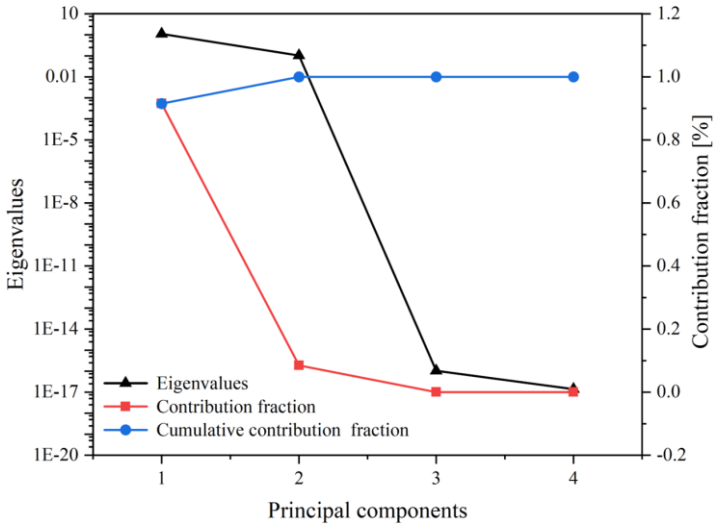

Figure 15. Principal component eigenvalues and contribution fractions.

The noise prediction accuracy is negatively correlated with factors B, C, and D for the first principal component of PCA (since a smaller integrated optimal metric indicates better noise evaluation, while higher

levels of B, C, and D result in larger integrated optimal metrics). On the other hand, factor A shows a positive correlation with noise prediction accuracy. For the second principal component, all factors exhibit a negative correlation with noise prediction accuracy. By combining the contribution fractions and expressions of the principal components, the final comprehensive evaluation function is derived as

$$Y_Z = -0.3568x_1 + 0.061304x_2 + 0.229483x_3 + 0.812946x_4 \quad (17)$$

B, C, and D demonstrate a negative correlation with noise prediction accuracy in the integrated optimal metric, while A exhibits a positive correlation. This observation aligns with the findings of the first principal component, which carries a weight of 91% in the integrated optimal metric. Furthermore, the PCA comprehensive evaluation function provides a quantitative analysis of each factor's influence on the noise prediction results. Specifically, the influence weights of A, B, C, and D on the noise prediction accuracy are 0.3568, 0.061304, 0.229483, and 0.812946, respectively. The size of domain D has the greatest impact on the accuracy of noise prediction, with a 1% change resulting in an approximately 81.3% alteration in the comprehensive evaluation function. The sensitivity

ranking of each factor to the noise prediction accuracy is D>A>C>B.

4.3. Evaluation of optimal mesh refinement strategy

The four aforementioned mesh refinement strategies are individually simulated and compared, and the obtained values of the noise optimization metrics are depicted in Figure 16. CaseZ1 demonstrates a less noticeable optimization effect on the TSP, with no significant reduction in the deviation between the predicted values of TST, broadband noise, and the experimental data. CaseZ2 exhibits a certain degree of optimization in Z2, reaching the lowest value of 3.27 dB. Simultaneously, it also leads to a significant reduction in Z1 and Z3. Its performance in Z1 and Z2 is unsatisfactory although CaseZ3 shows a minor reduction in broadband noise (Z3). CaseZtotal showcases a certain level of optimization effect on the three metrics, but fails to achieve the notable effect attained by CaseZ2. Overall, CaseZ2 exhibits the smallest integrated optimal metric, reaching the same score in Ztotal as Case9 with 15 million elements, reducing the element count by approximately 4 million and consuming fewer computational resources. Consequently, it is deemed the most effective

refinement strategy. Subsequent calculations and comparisons utilize the refinement scheme of CaseZ2, as it offers the highest accuracy in comprehensive aerodynamic noise prediction.

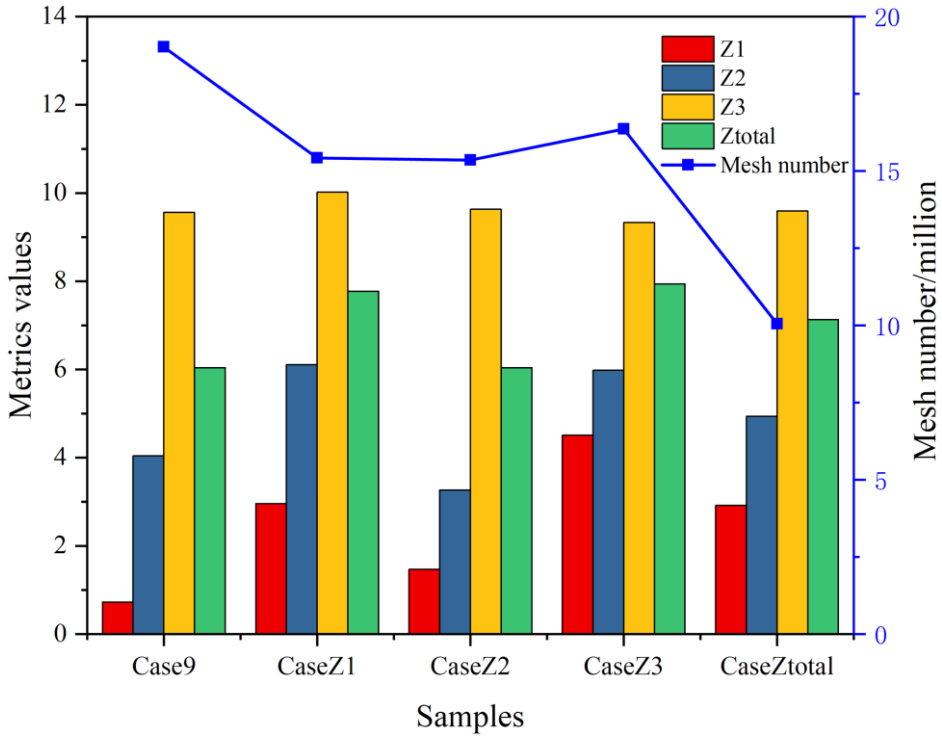

Figure 16. Optimization metrics values for prediction noise of mesh refinement scheme.

4.4. The influence of the thickness of first layer

The previously optimized refinement strategy, caseZ2, is utilized to investigate the impact of the Y+ value on the wall on the accuracy of aerodynamic noise prediction. Specifically, variations are only made to the thickness of first layer and total boundary layer. The aerodynamic noise

prediction accuracy is then examined for Y+ values around 1, 5, 10, 20, 30, and 50. Figure 17 illustrates the values of the optimization metrics for fan aerodynamic noise predicted with different Y+ values on the wall. There is a gradual increase in the deviation between the numerical and the experimental values as the Y+ value increases. It suggests that it is optimal to maintain Y+ near 1 on the blade surface when using the SST turbulence model. Figure 18 presents a comparison between the noise spectra of CaseY1 and CaseY50, predicted at point 2, and the corresponding experimental values. The predicted aerodynamic noise is greater in the low-frequency region around 1BPF irrespective of the Y+ value, as depicted by the shaded area in the figure. Both cases underestimate the noise in the noise spectrum above 1500Hz. Increasing the Y+ value enlarges the low-frequency component of the predicted noise while reducing the high-frequency part. Consequently, it leads to a wider discrepancy between the noise predicted by CaseY50 and the experimental data, which aligns with the increased values of the Z1 and Z3 metrics reflected in Figure 17. As for TST noise, the predicted noise peaks at 1BPF and 2BPF closely match the experimental values, while the amplitude of

the predicted noise at 3BPF is relatively large, and that at 4BPF is small. Raising the Y+ value introduces greater deviations between the TST noise and the experimental values, indicating that increasing the Y+ value results in higher values for the aforementioned three metrics, thereby reducing the accuracy of the predicted noise. The presence of some spikes in the predicted noise, as observed in Figure 18, can be attributed to the relatively coarse resolution. The issue can be resolved by further increasing the frequency resolution of the predicted noise.

Figure 19 displays the distribution of dipole sound source intensity on the blade surface under different Y+ values. The uniformity of sound source distribution on the stator hub near the rotor (represented by the black box in the figure) increases with the increment of Y+ value. It should be noted that the rotor wakes leaves distinctive "marks" on the stator hub due to the slightly larger diameter of the stator hub compared to the rotor, as depicted in Figure 19 (a) and (b). It indicates that as the Y+ value continues to rise, capturing the interaction between the rotor wake and the stator hub becomes increasingly challenging. The complex flow patterns (highlighted in red circles) between the end of the stator hub and the stator are smoothed

out as the Y+ value increases. An increasing Y+ value hampers the ability to capture the interaction between the hub and intricate flows, thereby diminishing the detection of dipole sound sources associated with these interferences and subsequently reducing the accuracy of aerodynamic noise prediction. The dipole sound sources near the leading edge of the rotor and the blade tip exhibit relatively high intensities, exceeding 90 dB. The latter is attributed to the tip clearance of the axial flow fan in the study, which reaches 5 mm. The leading edge and suction surface of the stator also serve as significant dipole sound sources. The former arises from the periodic impingement of the rotor wakes, while the latter experiences direct impacts from the rotor wakes, with both phenomena originating from the rotor-stator interaction.

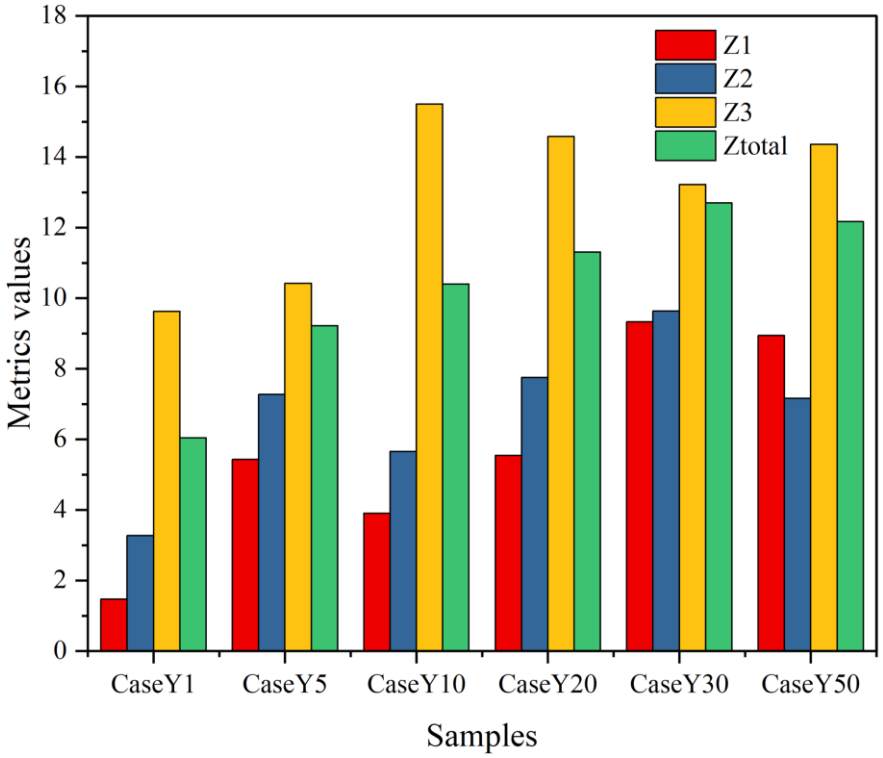

Figure 17. The influence of Y+ value on the prediction accuracy.

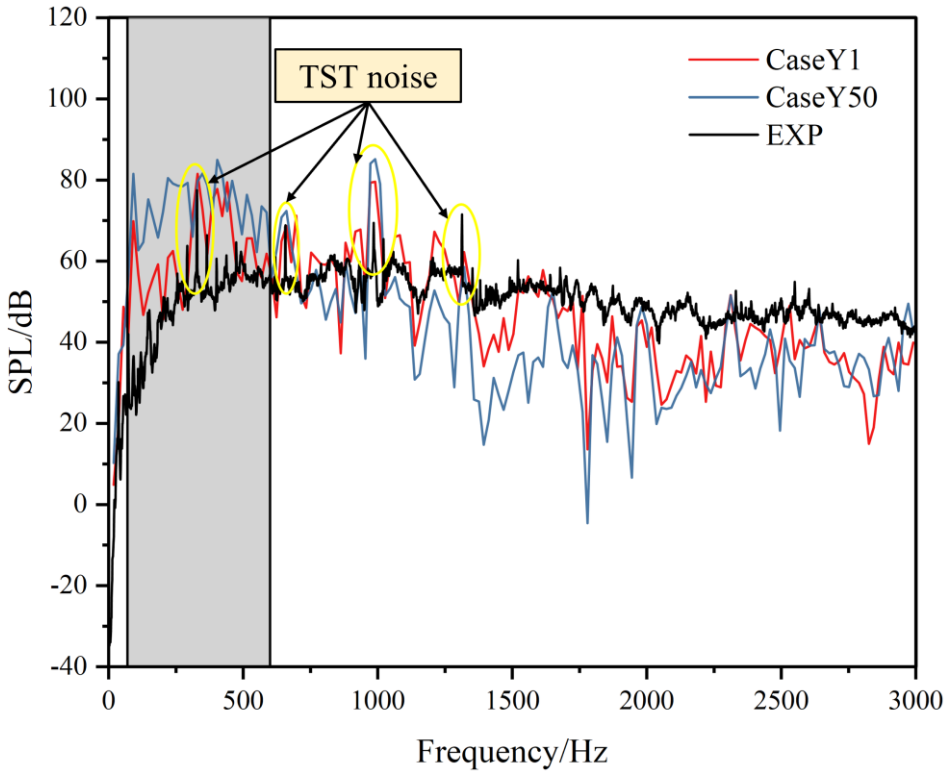

Figure 18. Comparison of noise spectrum predicted by Y+ values of 1 and 50 with experimental data.

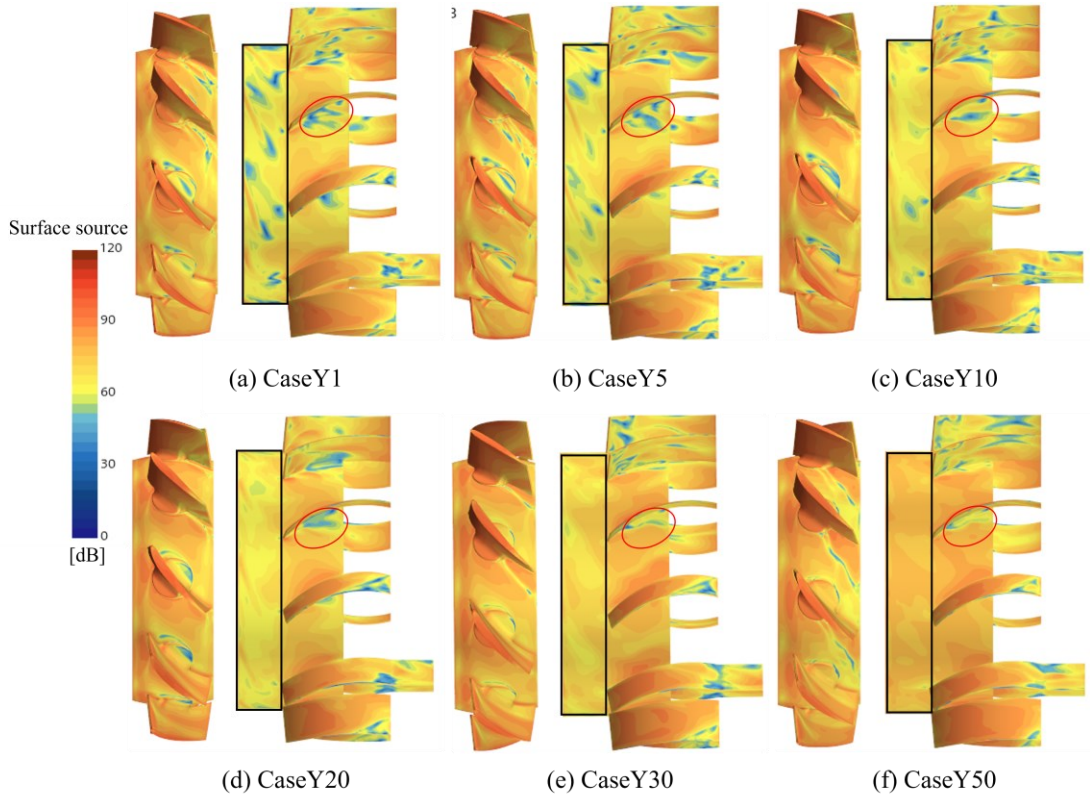

Figure 19. Dipole sound source intensity distribution on blade surface with different Y+ values.

4.5. The influence of the turbulence models

The optimal refinement strategy called CaseZ2, obtained in the previous study, is employed to investigate the influence of different turbulence models on the prediction accuracy of fan aerodynamic noise. Only the turbulence model is altered to explore the impact on the prediction accuracy of fan aerodynamic noise, including the K-E and SST models of URANS, the K-EDES and SSTDES models of DES, and the Smagorinsky-

LES, Dynamic Smagorinsky-LES, and WALELES models of LES. Table 10 presents the corresponding turbulence models and numerical prediction models. Figure 20 illustrates the optimized metric values of fan aerodynamic noise predicted by various turbulence models. The effect of different turbulence models on the TSP level (Z1) is relatively small, resulting in a constant value of approximately 1.7 dB, with no exceeding variation of 2 dB. The most accurate prediction of TST noise is achieved by the URANS SST model, where Z2 is only 2.7. Following this model are the Dynamic Smagorinsky-LES and WALELES models. The URANS models are not dominant concerning the broadband noise Z3 due to their assumption of time-averaged turbulent quantities in the flow. The DES models exhibit higher prediction accuracy for broadband noise, while the LES models perform less effectively than DES in predicting broadband noise. This observation may be attributed to the insufficient resolution near the wall in the current numerical simulation, failing to meet the stringent requirements of LES, as also noted by Lewis [18]. Even for the wall-modeled LES, specifically the WALELES model (CaseM7), the dimensionless wall distances S+ and R+ in the streamwise and third

directions still pose challenges in meeting the requirements, although the dimensionless wall distance Y+ of the grid in the normal direction meets the requirements. Regarding the integrated optimal metric Ztotal, the SST, K-EDES, and WALELES models (CaseM2, M3, and M7, respectively) demonstrate the best performance among the three categories of turbulence models (URANS, DES, and LES). The differences among these three optimal turbulence models are minimal, resulting in final aerodynamic noise scores of 6.04, 5.95, and 5.87, respectively.

Table 10. Correspondence between turbulence models and numerical models

Turbulence models	Numerical models
K-E	CaseM1
SST	CaseM2
K-EDES	CaseM3
SSTDES	CaseM4
Smagorinsky-LES	CaseM5
Dynamic Smagorinsky-LES	CaseM6
WALELES	CaseM7

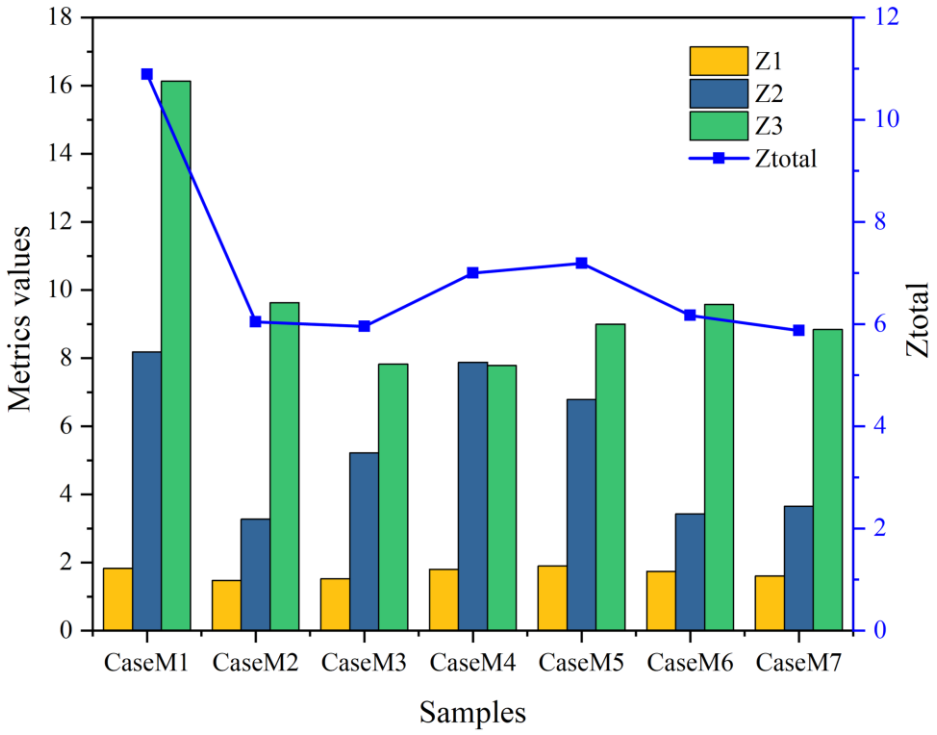

Figure 20. Influence of turbulence models on prediction accuracy of fan aerodynamic noise.

The comparison of CaseM3 and M7 with the experimental data is depicted in Figure 21. The substantial advantage of DES and LES, when compared to the URANS model in Figure 18, lies in the significantly improved prediction accuracy of broadband noise. The broadband noise of CaseM3 and M7 above 1000 Hz closely approximates the experimental values, albeit with occasional downward peaks at specific frequencies, attributed to the coarse frequency resolution of the numerical simulation. Satisfactory prediction results of DES and LES are observed for TST noise,

capturing frequency peaks with relatively close amplitudes. However, a gap still exists at the 4BPF, with the numerical simulation predicting lower magnitudes. Notably, LES exhibits better prediction performance for 4BPF compared to DES, displaying a smaller deviation from the experimental values. Some extra peaks are present in both the numerical simulation and experimental noise data, appearing at frequencies distinct from TST noise (as indicated by the red circle in the figure). These additional peaks are also observed in the SST turbulence model illustrated in Figure 18. The mechanism behind their generation will not be extensively investigated due to the focus of this paper. It is worth noting that the noise amplitude predicted by the numerical simulation is significantly higher than the experimental measurements at these frequencies, with multifaceted factors contributing to this discrepancy. Influences such as obstacle reflection in the experimental measurement environment and inaccurate modeling of the fan's complex geometric structure are important factors that contribute to the overestimation in the numerical predictions.

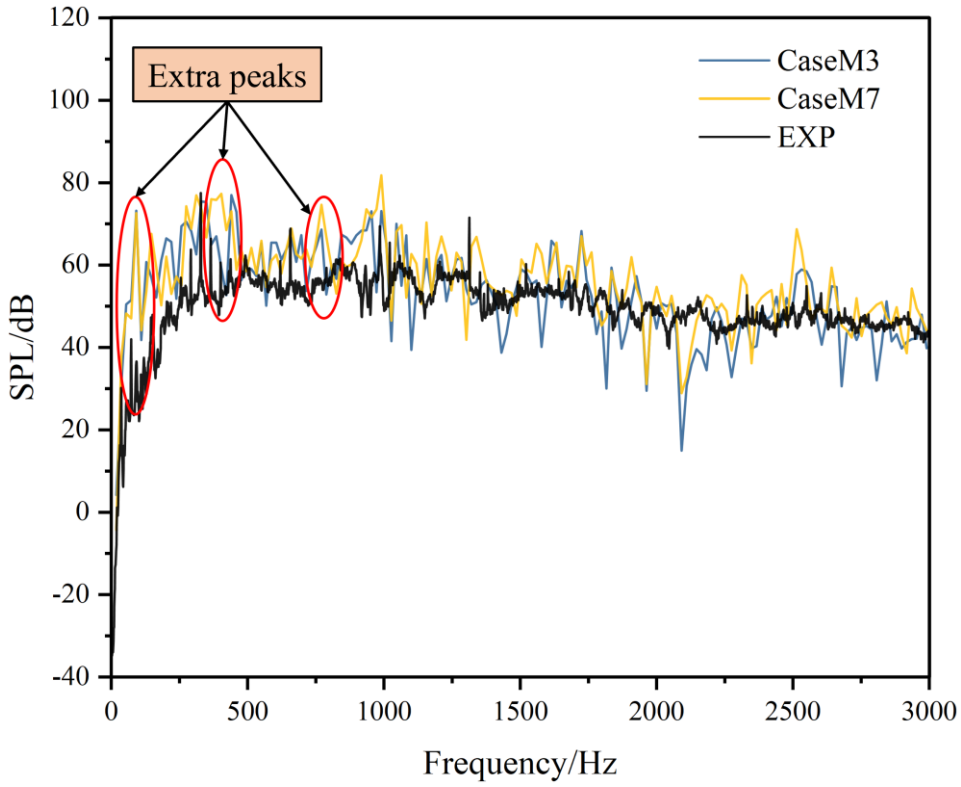

Figure 21. Comparison of the noise spectrum predicted by CaseM3 and M7 with the experimental data.

Figure 22 presents the instantaneous entropy distribution in the 50% span of the fan for CaseM1, M3, and M7 to visually compare the differences between URANS, DES, and LES turbulence models. The URANS model represents the average flow field within the fan and lacks the capability to capture the rotor wake and vortex structure. In contrast, DES and LES models simulate the rotor wake in a more refined manner, ensuring accurate dissipation as it propagates downstream. Broadband noise is directly influenced by the turbulence state affecting the flow state

of the stator row. Therefore, the accurate simulation of typical turbulent variables, such as the turbulent kinetic energy of the rotor wake and flow feature size, determines the prediction accuracy of broadband noise. The instantaneous results from DES and LES reveal a turbulent boundary layer on the suction surface of the rotor near the midchord length, while a quasi-laminar flow is observed on the pressure surface. The boundary layer thickness increases along the flow direction. This leads to the formation of the turbulent rotor wake dissipated in the progresses downstream that eventually impacts the stator. Previous research [54, 55] indicates that the rotor wake's effect on the stator does not induce a transition to turbulent flow at the leading edge of the stator. However, the large bending angle of the fan stator directly generates a substantial vortex on the suction surface in this study, consuming significant energy and contributing to the fan's low efficiency. Subsequently, the wake of the rotor and the vortices generated by the stator further develop downstream between the stator channels, forming a turbulent stator wake at the trailing edge. DES and LES effectively capture these turbulent features, leading to accurate predictions of broadband noise. As the stator wake continues downstream,

the simulation of the vortex becomes coarser after passing through the refinement region. It does not impact the prediction accuracy of broadband noise because the core region's refinement is sufficient to capture the turbulence characteristics of the stator region.

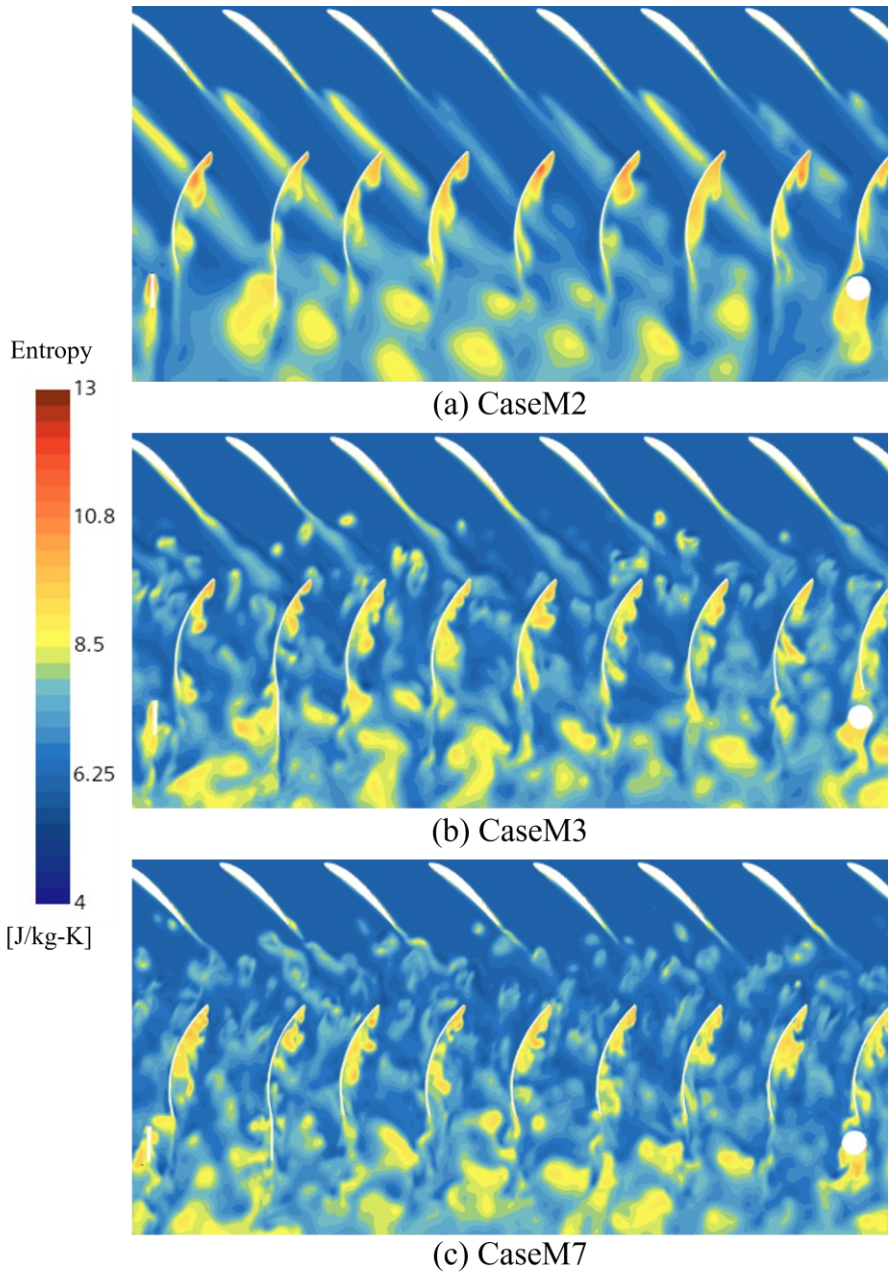

Figure 22. Instantaneous entropy distribution of three optimal turbulence models in

50% span

5. Conclusions

The paper addresses the main objective by identifying a set of schemes capable of accurately predicting the aerodynamic noise, including broadband noise, in fan or turbomachinery. Numerous calculations and experimental data are utilized to determine these schemes. The mesh refinement scheme employed is CaseZ2, ensuring a Y+ value close to 1 on the wall surface. The turbulence models chosen are K-EDES or WALELES, which exhibit accurate prediction capabilities for turbomachinery aerodynamic noise, specifically in simulating broadband noise. The SST model is recommended if a URANS model must be selected. However, it is important to acknowledge the limitations of this research. Only a detailed quantitative analysis of the mesh size in the four refinement areas on noise prediction accuracy is conducted, while the evaluation system not encompass the influence of wall Y+ and turbulence models. It should be noted that there exists a correlation between turbulence models, wall Y+, and mesh size. Nevertheless, it is impractical to incorporate all these factors

into the OED/PCA evaluation system for quantitative and related analysis. The computational workload of this study is already substantial, taking two months to simulate on four servers equipped with 64-core AMD EPYC CPUs.

The paper introduces a joint objective evaluation method based on OED/PCA to investigate the influential factors on the prediction accuracy of fan aerodynamic noise. Specifically, the study focuses on the CFD mesh refinement size of the fan's core area. The evaluation method does not encompass other factors such as wall Y+ value and turbulence models, which are separately analyzed using the control variable method. Consequently, a set of schemes capable of accurately predicting fan aerodynamic noise is established. The key findings of this investigation can be summarized as follows.

1. In response to the current issue of subjective and single-metric noise evaluation in numerical simulations, an enhanced comprehensive evaluation method is developed by combining OED and PCA. The method incorporates additional metrics to enable a detailed quantitative analysis of the influence of key factors on the accuracy of aerodynamic

noise prediction from various perspectives.

2. The influence of CFD mesh size in the core area of the fan on the accuracy of aerodynamic noise is initially analyzed using the OED method. It is determined that the mesh size of the stator wake (D area) has the most significant impact on the accuracy of noise prediction. Subsequently, the initial mesh refinement strategy is derived based on the three noise optimization metrics of TSPZ1, TSTZ2, and broadband noise Z3, respectively.
3. A new integrated optimal metric Ztotal is formed using the PCA method by incorporating the three optimization metrics. The contribution rate of each metric to Ztotal is provided. The proposed evaluation method is utilized to quantitatively analyze the impact of CFD mesh size in the core area on Ztotal, and a sensitivity ranking of each area size to noise is determined as D>A>C>B. The influence weight of D on noise accuracy is calculated to be 81.3%.
4. The four initially obtained refinement strategies are subjected to detailed analysis and research using the proposed optimization metrics. It is observed that the CaseZ2 refinement strategy for TST noise can

achieve an equivalent score to that of 19 million elements, utilizing only 15 million elements, which is identified as the optimal solution obtained in this research.

5. The impacts of the wall Y+ value and the turbulence models on the accuracy of noise prediction are individually investigated through the utilization of the control variable method. The findings indicate that as the Y+ value increases, the disparity between the numerical prediction noise and the experimental data also increases. It is recommended to maintain the Y+ value around 1. DES and LES demonstrate effective capabilities in simulating the turbulent flow characteristics both upstream and downstream of the stator, enabling accurate simulation of broadband noise. Ultimately, a set of numerical simulation schemes is developed to achieve precise prediction of fan aerodynamic noise.

6. Acknowledgment

This work was supported by Fundamental Research Funds for the Central Universities (3072022TS0307) and National Science and Technology Major Project (HT-J2019-II-0013-0034).

References

[1] V.S. Bjorn, A Research Plan: The Relationship of Ear, Head, & Neck Anthropometry to Military Hearing Protection Effectiveness, SAFE Association 39th Annual Symposium, September 17, 2001 - September 19, 2001, Survival and Flight Equipment Association (SAFE), Nashville, TN, United states, 2001, pp. 231-236.

[2] J. Hofmann, C. Thiebaut, M. Riondet, P. Lhuissier, S. Gaudion, M. Fivel, Comparison of acoustic and hydrodynamic cavitation: Material point of view, Physics of Fluids 35(1) (2023).

[3] D.L. Huff, NASA Glenn's contributions to aircraft engine noise research, Journal of Aerospace Engineering 26(2) (2013) 218-250.

[4] C.-C. Ye, P.-J.-Y. Zhang, Z.-H. Wan, D.-J. Sun, X.-Y. Lu, Numerical investigation of the bevelled effects on shock structure and screech noise in planar supersonic jets, Physics of Fluids 32(8) (2020).

[5] U. Piomelli, Large eddy simulations in 2030 and beyond, Philosophical Transactions of the Royal Society A: Mathematical, Physical and

Engineering Sciences 372(2022) (2014).

[6] X. Wen, S. Gierth, M. Rieth, J.H. Chen, C. Hasse, Large-eddy simulation of a multi-injection flame in a diesel engine environment using an unsteady flamelet/progress variable approach, Physics of Fluids 33(10) (2021).

[7] J. Williams, U. Wolfram, A. Ozel, Neural stochastic differential equations for particle dispersion in large-eddy simulations of homogeneous isotropic turbulence, Physics of Fluids 34(11) (2022).

[8] M. Ottersten, H.D. Yao, L. Davidson, Tonal noise of voluteless centrifugal fan generated by turbulence stemming from upstream inlet gap, Physics of Fluids 33(7) (2021).

[9] C. Polacsek, A. Cader, M. Buszyk, R. Barrier, F. Gea-Aguilera, H. Posson, Aeroacoustic design and broadband noise predictions of a fan stage with serrated outlet guide vanes, Physics of Fluids 32(10) (2020).

[10] J. Wang, K. Ishibashi, T. Ikeda, T. Fujii, T. Nakata, H. Liu, Morphological effects of leading-edge serrations on the acoustic signatures of mixed flow fan, Physics of Fluids 34(4) (2022).

[11] Y. Wang, F. Lv, L. Sun, M. Gao, Numerical simulation of aerodynamic

noise for the two-stage adjustable-blade axial-flow fan, Physics of Fluids 34(9) (2022).

[12] J. Al-Am, V. Clair, A. Giauque, J. Boudet, F. Gea-Aguilera, Aeroacoustic analysis of the tip-leakage flow of an ultrahigh bypass ratio fan stage, Physics of Fluids 35(4) (2023).

[13] C.P. Arroyo, T. Leonard, M. Sanjose, S. Moreau, F. Duchaine, Large eddy simulation of a scale-model turbofan for fan noise source diagnostic, Journal of Sound and Vibration 445 (2019) 64-76.

[14] S. Hamada, S. Nakashima, C. Kato, Y. Yamade, Asme, Aerodynamic noise simulation of propeller fan by large eddy simulation, 5th Joint ASME/JSME Fluids Engineering Summer Conference, San Diego, CA, 2007, pp. 183-190.

[15] N. Sinha, J. Erwin, C. Kannepalli, LES Predictions of Noise Emissions From a Low-Bypass Ratio Military Gas Turbine Engine, Journal of Engineering for Gas Turbines and Power-Transactions of the Asme 133(4) (2011).

[16] S. Tomimatsu, Y. Yamade, Y. Hirokawa, N. Nishikawa, Prediction of flow field and aerodynamic noise of jet fan using large eddy

simulation, Journal of Visualization 15(3) (2012) 253-259.

[17] S. Wasala, Y. Xue, L. Stevens, T. Wiegandt, T. Persoons, Numerical simulations of flow induced noise from a dual rotor cooling fan used in electronic cooling systems, 50th International Congress and Exposition of Noise Control Engineering, INTER-NOISE 2021, August 1, 2021 - August 5, 2021, The Institute of Noise Control Engineering of the USA, Inc., Washington, DC, United states, 2021, p. Pliteq.

[18] D. Lewis, S. Moreau, M.C. Jacob, M. Sanjose, ACAT1 Fan Stage Broadband Noise Prediction Using Large-Eddy Simulation and Analytical Models, Aiaa Journal 60(1) (2022) 360-380.

[19] C.D. Argyropoulos, N.C. Markatos, Recent advances on the numerical modelling of turbulent flows, Applied Mathematical Modelling 39(2) (2015) 693-732.

[20] S.J. Lawson, G.N. Barakos, Review of numerical simulations for high-speed, turbulent cavity flows, Progress in Aerospace Sciences 47(3) (2011) 186-216.

[21] P. Spalart, W.H. Jou, M. Strelets, S. Allmaras, Comments on the

feasibility of LES for wings, and on a hybrid RANS/LES approach, (1997) 137-147.

[22] Y. Yang, L. Zheng, Assessment of nonlinear-low Reynolds number/detached eddy simulation turbulence model for wake flow field simulation of a realistic automotive model, Physics of Fluids 35(1) (2023).

[23] J. Gong, J. Ding, L. Wang, Propeller-duct interaction on the wake dynamics of a ducted propeller, Physics of Fluids 33(7) (2021).

[24] Y. Liu, Z. Zhou, L. Zhu, S. Wang, Numerical investigation of flows around an axisymmetric body of revolution by using Reynolds-stress model based hybrid Reynolds-averaged Navier-Stokes/large eddy simulation, Physics of Fluids 33(8) (2021).

[25] G. Nasif, R. Balachandar, R.M. Barron, Influence of bed proximity on the three-dimensional characteristics of the wake of a sharp-edged bluff body, Physics of Fluids 31(2) (2019).

[26] P.R. Spalart, Detached-Eddy Simulation, Annual Review of Fluid Mechanics 41 (2009) 181-202.

[27] L. Wang, T. Wu, J. Gong, Y. Yang, Numerical analysis of the wake

dynamics of a propeller, Physics of Fluids 33(9) (2021).

[28] A. Wohlbrandt, C. Kissner, S. Guerin, Impact of cyclostationarity on fan broadband noise prediction, Journal of Sound and Vibration 420 (2018) 142-164.

[29] M.-J. Park, D.-J. Lee, Sources of broadband noise of an automotive cooling fan, Applied Acoustics 118 (2017) 66-75.

[30] W. Kim, N. Hur, W.-H. Jeon, Numerical analysis of unsteady flow field and aeroacoustic noise of an axial flow fan, Korean Society of Computatuonal Fluids Engineering 15(4) (2010) 60-66.

[31] S.M. Grace, Fan broadband interaction noise modeling using a low-order method, Journal of Sound and Vibration 346(1) (2015) 402-423.

[32] S.M. Grace, J. Maunus, D.L. Sondak, Effect of CFD wake prediction in a hybrid simulation of fan broadband interaction noise, 17th AIAA/CEAS Aeroacoustics Conference 2011 (32nd AIAA Aeroacoustics Conference), June 5, 2011 - June 8, 2011, AIAA International, Portland, OR, United states, 2011, p. American Institute of Aeronautics and Astronautics (AIAA).

[33] J. Maunus, S. Grace, D. Sondak, V. Yakhot, Characteristics of

turbulence in a turbofan stage, Journal of Turbomachinery 135(2) (2013).

[34] R. Jaron, H. Herthum, M. Franke, A. Moreau, S. Guerin, Impact of turbulence models on rans-informed prediction of fan broadband interaction noise, 12th European Conference on Turbomachinery Fluid Dynamics and Thermodynamics, ETC 2017, April 3, 2017 - April 7, 2017, KTH Royal Institute of Technology, Stockholm, Sweden, 2017.

[35] S. Guerin, C. Kissner, P. Seeler, R. Blazquez, P. Carrasco Larana, H. de Laborderie, D. Lewis, P. Chaitanya, C. Polacsek, J. Thisse, ACAT1 benchmark of RANS-informed analytical methods for fan broadband noise prediction: Part II-influence of the acoustic models, Acoustics 2(3) (2020) 617-649.

[36] C. Kissner, S. Guerin, P. Seeler, M. Billson, P. Chaitanya, P.C. Larana, H. de Laborderie, B. Francois, K. Lefarth, D. Lewis, G.M. Villar, T. Node-Langlois, ACAT1 benchmark of RANS-informed analytical methods for fan broadband noise prediction-Part I-influence of the RANS simulation, Acoustics 2(3) (2020) 539-578.

[37] M.S. Abdullah, M.H.H. Ishak, F. Ismail, Performance improvement of the Savonius turbine using a novel augmentation device with the Taguchi optimization method, Physics of Fluids 35(1) (2023).

[38] Q. Jing, Y. Dong, J. Liu, H. Li, Y. Liu, S. Zhang, Analysis and Optimization Study of Piston in Diesel Engine Based on ABC-OED-FE Method, Mathematical Problems in Engineering 2021 (2021).

[39] D. Lin, M. He, M. Xu, C. Zhou, X. Chen, An updated numerical model of fracture fluid loss coupled with wellbore flow in managed pressure drilling, Physics of Fluids 35(5) (2023).

[40] Y. Zhang, J. Ruan, X. Niu, T. Tan, W. Wen, Optimization analysis study of a multi-stage SICG based on OED, IEEE Transactions on Dielectrics and Electrical Insulation 22(4) (2015) 2073-2080.

[41] Y. Liu, X. Chu, W. Wang, B. Weigand, Large-eddy simulation, convective instability, and modal causality of coaxial supersonic air-water jets considering a swirl effect, Physics of Fluids 35(6) (2023).

[42] K. Taira, S.L. Brunton, S.T.M. Dawson, C.W. Rowley, T. Colonius, B.J. McKeon, O.T. Schmidt, S. Gordeyev, V. Theofilis, L.S. Ukeiley, Modal analysis of fluid flows: an overview AIAA Journal 58(11)

(2020) AU9-AU9.

[43] K. Taira, M.S. Hemati, S.L. Brunton, Y. Sun, K. Duraisamy, S. Bagheri, S.T.M. Dawson, C.-A. Yeh, Modal analysis of fluid flows: applications and outlook, AIAA Journal 58(3) (2020) 998-1022.

[44] G. Zhang, Z. Wang, H. Huang, H. Li, T. Sun, Comparison and evaluation of dimensionality reduction techniques for the numerical simulations of unsteady cavitation, Physics of Fluids 35(7) (2023).

[45] C. Eckart, G. Young, The approximation of one matrix by another of lower rank, Psychometrika 1(3) (1936) 211-218.

[46] C. Polacsek, S. Burguburu, S. Redonnet, M. Terracol, Numerical simulations of fan interaction noise using a hybrid approach, AIAA Journal 44(6) (2006) 1188-1196.

[47] B.-B. Hu, H. Ouyang, Y.-D. Wu, G.-Y. Jin, X.-Q. Qiang, Z.-H. Du, Numerical prediction of the interaction noise radiated from an axial fan, Applied Acoustics 74(4) (2013) 544-552.

[48] J. Zhang, W. Chu, H. Zhang, Y. Wu, X. Dong, Numerical and experimental investigations of the unsteady aerodynamics and aero-acoustics characteristics of a backward curved blade centrifugal fan,

Applied Acoustics 110 (2016) 256-267.

[49] H. Lu, Y. Xiao, Z. Liu, Y. Yuan, Simulation and experimental research on aerodynamic noise of gas turbine 1.5-stage axial compressor, Applied Acoustics 192 (2022) 108722.

[50] M.-S. Shi, P.-A. Chi, W.-L. Chen, Prediction on turbomachinery flows using advanced turbulence models, Journal of Aeronautics, Astronautics and Aviation 51(2) (2019) 159-170.

[51] J. Yang, H. Wu, Explicit coupled solution of two-equation k- SST turbulence model and its application in turbomachinery flow simulation, Hangkong Xuebao/Acta Aeronautica et Astronautica Sinica 35(1) (2014) 116-124.

[52] Y. Anand, S.K. Verma, S. Anand, Ashrae, Transient 3-D modelling of ceiling fan for achieving thermal comfort, Building Performance Analysis Conference and SimBuild, Chicago, LA, 2018, pp. 197-204.

[53] S.M. Sajadmanesh, M. Mojaddam, A. Mohseni, A. Nikparto, Numerical identificaticin of separation bubble in.an ultra-high-lift turbine cascade using URANS simulation and proper orthogonal decomposition, Aerospace Science and Technology 93 (2019).

[54] J. de Laborderie, S. Moreau, A. Berry, Compressor stage broadband noise prediction using a large-eddy simulation and comparisons with a cascade response model, 19th AIAA/CEAS Aeroacoustics Conference, May 27, 2013 - May 29, 2013, AIAA International, Berlin, Germany, 2013, p. 41.

[55] N. Gourdain, Prediction of the unsteady turbulent flow in an axial compressor stage. Part 2: Analysis of unsteady RANS and LES data, Computers and Fluids 106 (2015) 67-78.